

# Mass Models for Spiral Galaxies from 2-D Velocity Maps

Eric I. Barnes, J. A. Sellwood, & Arthur Kosowsky

*Department of Physics & Astronomy, Rutgers University, Piscataway, NJ 08854*

barnesy@physics.rutgers.edu

sellwood@physics.rutgers.edu

kosowsky@physics.rutgers.edu

## ABSTRACT

We model the mass distributions of 40 high surface brightness spiral galaxies inside their optical radii, deriving parameters of mass models by matching the predicted velocities to observed velocity maps. We use constant mass-to-light disk and bulge models, and we have tried fits with no halo and with three different halo density profiles. The data require a halo in most, but not all, cases, while in others the best fit occurs with negligible mass in the luminous component, which we regard as unphysical. All three adopted halo profiles lead to fits of about the same quality, and our data therefore do not constrain the functional form of the halo profile. The halo parameters display large degeneracies for two of the three adopted halo functions, but the separate luminous and dark masses are better constrained. However, the fitted disk and halo masses vary substantially between the adopted halo models, indicating that even high quality 2-D optical velocity maps do not provide significant constraints on the dark matter content of a galaxy. We demonstrate that data from longslit observations are likely to provide still weaker constraints. We conclude that additional information is needed in order to constrain the separate disk and halo masses in a galaxy.

*Subject headings:* galaxies:fundamental parameters — galaxies:kinematics and dynamics — galaxies:dark matter — galaxies:stellar content

## 1. Introduction

The mass of a galactic stellar population has proved to be a particularly difficult quantity to determine. In principle, an accurate value would place a constraint on the star formation history, stellar mass function, and metallicity. But it is perhaps more important for dynamics because it affects estimates of the dark matter content of the inner parts of galaxies. There are two possible approaches to estimating the stellar mass: dynamical measurements and comparison of the observed broad-band colors or spectra with theoretical predictions from population synthesis.

Theoretical models to synthesize a stellar population (*e.g.*, Arimoto & Yoshii 1986; Bruzual & Charlot 1993; Worthey 1994; Bell *et al.* 2003) use established stellar models and assumptions about

the likely mass function, star formation history, etc. to predict the luminosity in a broad-band color. The expected luminosity in almost any color band is insensitive to the low-mass slope of the adopted mass function, since large proportions of low-mass stars can be added or removed with little effect on the total luminosity. The resulting mass-to-light values,  $\Upsilon$ , are thought to be reliable to within a factor of 2 (Bell & de Jong 2001).

The dynamical approach is scarcely more successful. The typical circular flow pattern of gas in a spiral galaxy affords a rather precise estimate of the overall mass profile within the radial range explored by the data. But it is much harder to determine the fraction of the enclosed mass that comes from the starlight, since an unknown fraction of dark matter is also expected to contribute. A common simplifying assumption is that the disk mass

profile traces that of the disk light with a constant, but unknown,  $\Upsilon$ . But van Albada *et al.* (1985) and Lake & Feinswog (1989) stress that, for an axisymmetric flow pattern, the disk and halo masses are almost completely degenerate, even for galaxies with the best available rotation curve data from neutral hydrogen observations.

An additional factor that contributes to this difficulty is the unknown density profile of the dark matter halo. Previous studies have tried a number of functional forms, some motivated by cosmological simulations, but with no decisive conclusions (*e.g.*, Navarro 1998; Jimenez, Verde & Oh 2002). It is scarcely surprising that very weak constraints result from fitting a 1-D rotation curve as the sum of a contribution from the luminous matter, with an unknown mass scaling, plus a contribution from dark matter with both an unknown functional form and an unknown density normalization.

Weiner, Sellwood & Williams (2001b), Weiner (2003), and Kranz, Slyz & Rix (2003) were able to obtain more precise estimates (within  $\sim 10\%$ , Weiner *et al.* 2001b) of the stellar disk mass through modeling the non-axisymmetric flow pattern in disk galaxies. These were time-consuming studies, requiring a large grid of hydrodynamical simulations over the two unknowns,  $\Upsilon$  and the pattern speed of the bar or spiral. Alternatively, Bottema (1997) measures the velocity dispersion of the stars in the disk, to obtain a disk mass estimate (see also Verheijen *et al.* 2003). While these more challenging methods may yet be needed to break the disk-halo mass degeneracy, we here examine the question of whether fitting simple axisymmetric models to high-quality, 2-D optical velocity maps offers any tighter constraints over previous attempts at fitting 1-D rotation curves from longslit data or lower-resolution 2-D maps from aperture synthesis.

Velocity maps at low spatial resolution have long been available from neutral hydrogen aperture synthesis observations (*e.g.*, Bosma, van der Hulst & Sullivan 1977). More recently, velocity maps have become available at very high spatial resolution from mm-wave observations of molecular gas (Jogee *et al.* 2002; Sofue *et al.* 2003; Simon *et al.* 2003). Most optical data has continued to be obtained using longslit spectra (*e.g.*, Courteau 1997; Sofue & Rubin 2001; Vogt *et al.*

2004), but a few maps are available from integral field units; Corradi *et al.* (1991) and Palunas & Williams (2000) used Fabry-Perot maps, Andersen & Bershadsky (2002) have used fiber bundles, and the lens array spectrograph SAURON has been used to investigate early type galaxies (Davies *et al.* 2001).

Palunas & Williams present the largest sample of galaxies with homogeneously gathered Fabry-Perot maps and *I*-band photometry available so far. They showed that the inner rotation curves could be fitted by constant  $\Upsilon_I$  mass models and no dark matter, but with a rather wide range of  $\Upsilon_I$  values, when mass discrepancies in the outer parts were excluded from the fit. We here present a re-analysis of these galaxies to determine what can be concluded about the likely dark matter content of galaxies from fitting axisymmetric models to these data.

Our objective here is to try to determine whether our data place meaningful constraints on the dark matter content of the galaxies in our sample and whether one halo profile or another yields a significantly better fit within the radial range spanned by our data. These objectives are quite different from testing theoretical predictions from some model of galaxy formation.

We find that 2-D velocity maps do provide some advantage over 1-D rotation curves, in that they reduce the statistical uncertainties in estimated parameters. However, the disk mass, and therefore also the dark matter content of a galaxy, is still strongly dependent on the adopted halo density profile. We support these conclusions by fitting mass models to both the 2-D velocity map (§5) and to a 1-D rotation curve (§7) which we derive from data along only the major axis of our velocity maps.

## 2. Data

The data used in this paper were kindly provided by Povilas Palunas and Ted Williams (see Palunas & Williams 2000, hereafter PW, for a complete description of the data and reductions). We have *I*-band images and Fabry-Perot (hereafter FP) velocity maps for 74 high surface-brightness spiral galaxies. PW report the average seeing to be  $\approx 1.5''$ . We adopt the magnitudes, luminosities, and distances reported by

PW; distances are simply Hubble distances assuming  $H_0 = 75 \text{ km s}^{-1} \text{ Mpc}^{-1}$ .

Galaxies in this sample were selected to lie in a particular part of the sky, to be of later Hubble type, to not be classified as barred in the RC3 catalog (de Vaucouleurs *et al.* 1991) (although many are, in fact, barred), to not be obviously disturbed, to have a suitable angular size for the FP instrument, and to have redshifts in the range 4000 – 5000 km/s. The data were taken to obtain optical Tully-Fisher distances of galaxies to map departures from the Hubble flow in the general direction of the Great Attractor, which may have resulted in a somewhat larger than normal fraction of galaxies in clusters, although roughly half (35 of 74) are in the field. See § 4.1 for a discussion of the impact of the Great Attractor on the distances adopted for these galaxies. Apart from this, the sample seems unlikely to have any sinister biases relevant to their mass distributions.

We have created mass models for a subsample of 40 galaxies. The T-types of this subsample (from the RC3) range between 2 (Sab) and 10 (Irr) with most being 4-6 (Sbc-Sc). The radii at which the surface brightness is  $23.5 \text{ mag/arcsec}^2$   $R_{23.5}$  range from 24 to  $104''$ . Their average luminosity is  $3 \times 10^{10} L_\odot$  and ranges between  $8 \times 10^9$  and  $8 \times 10^{10} L_\odot$ . The average I-band central surface brightness is  $19.6 \mu$ , with the brightest galaxy at  $18.3 \mu$  and the faintest at  $21.3 \mu$ . Maximum circular speeds for these galaxies range from approximately 100 to 300 km/s with an average of 170 km/s. The 34 galaxies in their sample which we have omitted from this study are listed in Table 1. The majority were discarded because they are close to edge-on, having inclinations greater than  $75^\circ$ , which raises a number of difficulties: (1) The finite thickness of their disks becomes a significant fraction of the projected minor-axis and invalidates our simple razor-thin disk model (see §3.1). (2) Extinction problems become severe, and dust corrections large and uncertain. (3) The velocity map is less well resolved, and gas emission on the minor axis can more easily skew the estimated velocity from the major axis, which could lead to an estimated rotation curve that may be more slowly rising than is really the case. A few galaxies were discarded for other reasons, such as a lack of kinematic data in their central regions.

We did not discard galaxies on the basis of their

morphology and have persisted in fitting axisymmetric models to a few that manifestly have strong bars. The reason for this is that almost all galaxies in the sample have weak non-axisymmetric features, and judgements of which galaxies to discard would have been arbitrary and subjective. Modeling of the non-axisymmetric flow pattern would be superior, but it is a major task for even one galaxy (Weiner, Sellwood & Williams 2001b; Kranz, Slyz & Rix 2003) which we do not attempt here.

Throughout this paper, we fix the position angle  $\phi_0$ , inclination angle  $i$ , and systemic velocity  $v_s$  of each galaxy at the values deduced from earlier fits of axisymmetric flow patterns to our kinematic data (Barnes & Sellwood 2003). Briefly, we found the values of these parameters that minimized  $\chi^2$  between the 2-D velocity map from the FP data and a planar axisymmetric flow pattern. The fit therefore also yields a set of mean orbital speeds, and their uncertainties, at equally-spaced radii which we show as the “data” in subsequent figures. Since we fit axisymmetric mass models, we could, in principle, fit this 1-D rotation curve, which is basically the speed averaged in annular bins, provided we compute the weights correctly. However, our use of the biweight (§3.3) requires a fit to the full 2-D velocity map.

The use of kinematically-derived projection parameters is possible only because we have velocity maps. Rotation curves derived from long-slit observations must adopt inclination and major-axis position angles from the brightness distribution in the galaxy. We discuss how much this might affect the results in §7.

### 3. Methods

We build a mass model for each galaxy in our sample based on the measured light distribution in the I-band and a possible dark matter component, and then compare the 2-D velocity map expected from gas on circular orbits in our model with that observed from the H $\alpha$  emission.

We assume separate constant I-band mass-to-light,  $\Upsilon_I$ , for the disk and bulge components and neglect the possibility of  $\Upsilon_I$  gradients within each component. This is the usual assumption, despite established color gradients in galaxy disks (*e.g.*, de Jong 1996). We justify this assumption because the unknown correction for  $\Upsilon_I$  gradients will have

a small effect, as shown by Weiner *et al.* (2001a): the rotation curve shape for the disk is largely determined by the mass distribution in the dense inner parts, and changes to the density gradient at larger radii have a minor effect.

We also neglect any contribution from gas. In previous models where HI maps are available (*e.g.*, Broeils 1992; Verheijen 1997), the contribution from atomic gas to the rotation curve is generally very small in the inner parts, but rises toward the optical edge – to  $\lesssim 10\%$  of the central attraction in the most extreme case. Molecular gas is generally more concentrated towards the inner parts (*e.g.*, Regan *et al.* 2001) where its contribution may be somewhat larger, but we could not find any information on the molecular gas content of our galaxies. HI fluxes for 28 galaxies in our sample are available from NED.<sup>1</sup> Since we find gas mass fractions typical of the galaxies in these other studies, neglect of the gas contribution should result in only a slight systematic overestimate of the  $\Upsilon_I$  for the stellar component, unless the dark matter fraction is large.

We consider three different radial density profiles for the dark matter halo, which we assume to be spherical for simplicity. Two of our halo functions are standard: the pseudo-isothermal model with a constant-density core and a model with a broken power law; the third is a simple, scale-free power-law. Our objective is not to test any particular model of dark matter halo formation, but to determine how well our data constrain the halo contribution to the rotation curve in the disk plane. It is possible that halos are spheroidal, or even triaxial; the unknown shape of the halo may alter the inferred mean density profile slightly, but our data cannot constrain such subtleties. The calculation of the contribution to the circular velocity from a spherical halo model is straightforward.

### 3.1. Bulge-Disk Decomposition

Since we wish to allow the disk and the bulge to have separate  $\Upsilon_I$  values, we must separate the light distribution into these two components.

While we do this with care, the central attraction is not strongly sensitive to the precise decomposition, because we ensure that the  $\Upsilon_I$  of the two components in our models do not differ by a large factor. (We regard it as unlikely on physical grounds that  $\Upsilon_{B,I} \ll \Upsilon_{D,I}$ ; we discard all such solutions that emerge from an unconstrained minimization, often with  $\Upsilon_{B,I} \ll 0.1$ , and repeat the fit with the constraint that  $\Upsilon_{B,I} = \Upsilon_{D,I}$ .) We also ensure that all the light is included in one component or the other. Therefore the total luminous mass profile remains nearly the same no matter how the light is divided. The central attraction depends slightly on whether the mass is in a flat disk or a spheroid, with a maximum possible difference in circular speeds of  $\sim 15\%$  (Binney & Tremaine 1987, §2.6), and the fraction of bulge light is generally  $\lesssim 10\%$ . Thus the rotation curve shape from the luminous matter changes little as the division of light between the disk and bulge is adjusted.

Our decomposition method is described in Barnes & Sellwood (2003). Briefly, we assume the disk to be infinitesimally thin and axisymmetric, while the bulge is spheroidal, implying that our model isophotes for both components should be elliptical but have differing ellipticities,  $\epsilon$ . We assume the equatorial plane of the bulge is projected at the same inclination  $i$  and position angle  $\phi_0$  as the disk plane, which are the values derived from modeling the velocity map (§2). We allow the bulge to be either oblate or prolate. This choice varies from galaxy to galaxy, but most of our models are oblate. While we do not assume any functional form for the surface brightness profile of the disk – it is represented as a table of values – we follow PW and model the bulge as a sum (up to 3) of Gaussian light distributions. Detailed photometry of bulges with high spatial resolution (*e.g.*, Balcells *et al.* 2003) suggests that Gaussians may not be the most appropriate, but we find that a sum of three Gaussians can reproduce, *e.g.*, Sérsic profiles (Sérsic 1968) reasonably well. Though unorthodox, Gaussians have two advantages: the surface brightness is guaranteed to decrease faster than any likely disk profile at large radii, and they afford a convenient calculation of the central attraction (see §3.2). Our assumptions are less restrictive than in schemes that utilize specific functional forms for the luminous compo-

<sup>1</sup>The NASA/IPAC Extragalactic Database (NED) is operated by the Jet Propulsion Laboratory, California Institute of Technology, under contract with the National Aeronautics and Space Administration.

nents.

We first attempt to fit the photometric image with a disk alone. We then repeat the fit with the addition of a single Gaussian bulge component and compare the resulting  $\chi^2$  value with its value from the disk-only fit. (The dominant source of uncertainty is simple photon counting.) If the difference is significant, as indicated by an  $F$ -test, we continue to add a second and possibly a third component, accepting each only if the reduction in  $\chi^2$  is large enough that there is a better than 95% chance that the extra parameters are required. Our fitted photometric model typically has final reduced  $\chi_r^2$  (see § 3.3) in the range  $1 \lesssim \chi_r^2 \lesssim 1.5$ .

Our best-fit model has the following parameters; a disk ellipticity  $\epsilon_D$  that is related to the inclination  $i$  of the galaxy through  $\cos i = 1 - \epsilon_D$ , a set of disk intensities  $\{I_D\}$  at equally-spaced radii, the bulge ellipticity  $\epsilon_B$ , and the Gaussian central intensities  $\{I_B\}$  and scale lengths  $\{r_B\}$  of the bulge component(s).

### 3.2. Stellar Velocity Field Calculation

As mentioned earlier, a Gaussian form for the bulge simplifies the calculation of the central attraction. Since an axisymmetric Gaussian volume light distribution projects into a Gaussian surface brightness distribution (Stark 1977), the bulge luminosity density can be derived from the sum of the bulge components through

$$j(m^2) = \sqrt{\frac{f}{\pi}} \sum_n \frac{I_{B,n}}{r_{B,i}} e^{-m^2/r_{B,n}^2}, \quad (1)$$

where  $m = R^2 + (z/(1 - \epsilon_B))^2$ , and  $f = \cos^2 i + \sin^2 i/q_B^2$ . The apparent bulge axis ratio,  $q_{m,B}$ , is related to the bulge ellipticity,  $\epsilon_B = 1 - q_{m,B}$  and the intrinsic axis ratio of the bulge  $q_B$  is given by  $q_B^2 = (q_{m,B}^2 - \cos^2 i)/\sin^2 i$ . Finally, the bulge eccentricity  $e_B$  is given by,

$$e_B^2 = \begin{cases} 1 - q_B^2 & , \text{ oblate} \\ 1 - 1/q_B^2 & , \text{ prolate.} \end{cases}$$

The circular velocity in the equatorial plane due to the bulge is therefore (Binney & Tremaine 1987),

$$v_{c,B}^2(R) = 4\pi G \sqrt{1 - e_B^2} \Upsilon_{B,I} \int_0^R \frac{j(m^2)m^2 dm}{\sqrt{R^2 - m^2 e_B^2}}, \quad (2)$$

where  $\Upsilon_{B,I}$  is the mass-to-light ratio.

We evaluate disk circular velocities using the method based on Hankel transforms for a thin disk (Binney & Tremaine 1987),

$$v_{c,D}^2(R) = 2\pi \cos i G \Upsilon_{D,I} R \int_0^\infty \int_0^\infty \Sigma(R') J_0(kR') J_1(kR) R' k dk dR', \quad (3)$$

where  $\Sigma$  is the surface mass density,  $\Upsilon_{D,I}$  is the mass-to-light ratio, and  $J_0$  and  $J_1$  are cylindrical Bessel functions. The  $\cos i$  factor is an inclination correction for the surface brightness, that assumes a thin disk with no radial dependence to the extinction law. We solve Eq. (3) numerically, using a kernel approach. Since we neglect an (unknown) thickness correction, which would slightly reduce the circular speed for the same surface density, our  $\Upsilon_{D,I}$  values will be systematically underestimated.

### 3.3. Velocity Field Fitting

We fit our mass model to the galaxy by comparing the projected velocity map of our axisymmetric model to the observed 2-D velocity map from the FP data. As mentioned earlier, we adopt the kinematic projection angles from Barnes & Sellwood (2003), which we also used for the photometric model. We therefore have to minimize  $\chi^2$  for the remaining free parameters, which are the mass-to-light ratios for the disk  $\Upsilon_{D,I}$  bulge  $\Upsilon_{B,I}$  (if any), and parameters of the adopted halo.

The line-of-sight velocity at the  $k$ th-point in the projected disk plane predicted by our model is

$$v_{p,k} = v_s + v_{c,T} \frac{\sin i \cos i \cos(\phi - \phi_0)}{\sqrt{1 - \sin^2 i \cos^2(\phi - \phi_0)}}, \quad (4)$$

where  $v_{c,T}$  is the total circular speed from all mass components combined at that radius, and  $\phi_0$  and  $v_s$  are, respectively, the previously-determined major axis position angle and systemic velocity.

We evaluate the quantity  $z_k \equiv (v_{d,k} - v_{p,k})/\sigma_k$  at every pixel  $k$ , where  $v_{d,k}$  is the estimated line-of-sight velocity derived previously by PW from the FP data. The quantity  $\sigma_k$  is the statistical uncertainty, estimated by PW from the Voigt profile fit to the FP data cube, plus a small additional constant term of 7 km/s added in quadrature to represent the likely velocity dispersion of gas in a

disk.<sup>2</sup> The usual reduced  $\chi_r^2$  is therefore

$$\chi_r^2 = \frac{1}{\nu} \sum_{k=1}^N z_k^2, \quad (5)$$

where  $N$  is the number of pixels in the velocity map where we have an estimate of the line-of-sight velocity  $v_{d,k}$ , and the number of degrees of freedom,  $\nu = N -$  the number of parameters. We omit only those pixels where the Voigt-fitter failed to find a statistically significant velocity estimate from the FP velocity scan.

The value of  $\chi_r^2$  after minimization was unacceptably large for many galaxies. Inspection of the residual maps in these cases indicated that a small fraction of pixels, generally in the outer parts of the model, had differences of many  $\sigma_k$  between the model and data. The estimated velocities in these pixels generally differed significantly from those in the surrounding pixels, which is unlikely to be correct on physical grounds, and such outlying points occasionally exerted undue influence on the fitted parameter values. The spurious velocities in these pixels generally arise from falsely identified “emission lines” that formally have small errors, which could be caused by incompletely removed cosmic rays, for example. Non-circular streaming motions, particularly in bars, are further sources of major disagreement between our circular flow model predictions and the data.

We therefore adopt a robust estimation procedure using Tukey’s biweight, which reduces the influence of non-normally distributed errors on the fitted parameters (Press *et al.* 1992). In this case, we minimize the function

$$\chi_b^2 = \frac{1}{\nu} \sum_{k=1}^N \begin{cases} z_k^2 - \frac{z_k^4}{c^2} + \frac{z_k^6}{3c^4}, & |z_k| < c \\ \frac{c^2}{3}, & \text{otherwise} \end{cases} \quad (6)$$

where  $c$  is a constant. While data values that differ from the model prediction by  $\lesssim c\sigma_k/2$  contribute

<sup>2</sup>The intensity profile for any one pixel is broadened by the instrumental resolution, the intrinsic line-width from an individual HII region, and by the different velocities of the various HII regions along the line of sight. The Voigt fit corrects for the instrumental broadening, which has a FWHM  $\sim 125$  km/s. An estimated velocity uncertainty  $\lesssim 7$  km/s is therefore unreasonably low, and would give that datum too high a statistical weight in the fit. Furthermore, a single bright HII region that dominates the spectrum in one pixel may not be as close to the circular speed as indicated by the fitted error if it were in the wings of the turbulent velocity spread of the ISM.

to  $\chi_b^2$  almost exactly as for the conventional  $\chi_r^2$ , the contribution from data values that are farther from the model prediction by  $c\sigma_k$  does not change as the parameters are adjusted, and outlying data therefore do not influence the resulting parameter values. Press *et al.* (1992) recommend  $c = 6$ , but non-circular flow patterns in our galaxies suggest that a larger value would be more appropriate; after some experimentation we found  $c = 10$  still eliminated the influence of the extreme outlying velocities while allowing the great majority of the pixels to contribute to the fit with almost full weight.

Since all values of  $z_k$  are adjusted during the minimization, the impact of the biweight changes at every iteration. It is therefore inadequate to first derive a 1-D rotation curve to which we can fit our models; we must always fit to the entire 2-D velocity field.

### 3.4. Steepness of the Inner Rise

Many authors limit the upper value of  $\Upsilon$  so that the model rotation curve rises no more steeply than the observed curve in the inner parts. We, on the other hand, try to minimize the difference between the model and all the kinematic data without this constraint. As a result, our model rotation curve may exceed that observed in the central region.

We do not regard *mild* overfitting in this region as a serious shortcoming of our models. The reliability of the innermost data points has been discussed extensively in the context of halo constraints from LSB galaxies (van den Bosch *et al.* 2000; de Blok, McGaugh & Rubin 2001), and it is argued that every uncertainty leads to the observed velocity being lower than the true circular velocity. Non-circular motion, pressure support, seeing, and patchy emission can all lead to mild underestimation of the circular velocity in the observational data from the inner galaxy. (We have no potential error from slit misplacement, because the position of the rotation center is evident from our 2-D velocity maps.) Tests to model worse seeing gave results practically indistinguishable from those obtained with the original seeing. Patchy emission that is blurred by the seeing causes faint emission with the wrong velocity at points where no signal should have been detected.

Of these further sources of uncertainty, non-circular motions appear to have the greatest impact. Most galaxies in our sample have spiral patterns and some are clearly quite strongly barred. We have not, in this work, attempted to model the non-circular motions induced by such non-axisymmetric features, and continue to search for the best-fitting model with a circular flow pattern. This simplifying assumption clearly boosts  $\chi_b^2$ , but it can also introduce systematic errors. In particular, streaming motions in a bar generally cause the observed orbital speeds to be lower than circular, because the gas spends more time, and is more easily detected, near the apocenter of the streaming pattern where the speed must necessarily be lower than circular.

For these reasons, we consider a mild overfit in the central regions an acceptable result, and we accept a more significant overfit in galaxies having bars or other strong non-axisymmetric features.

#### 4. Stars-only Fits

We first fit the velocity maps with models based on the light distribution alone (stars-only fits). The fitting parameter is  $\Upsilon_{D,I}$ , with a second  $\Upsilon_{B,I}$  parameter when a bulge is included. We list the best-fit parameters along with their uncertainties (estimated as described below) in Table 2.

Figure 1 shows our results for four representative galaxies. The mean orbital speed as a function of radius is shown by the points with error bars; these values are deduced from the 2-D FP velocity map by the method described in Barnes & Sellwood (2003). The solid line in these Figures shows the rotation curve of our best-fit, stars-only, model; the disk contribution is the dashed line, and the bulge contribution (if present) is the dash-dotted line. The four panels in Figure 1 show examples of different types of behavior.

PW found that the large majority of galaxies in their sample could be modeled adequately without dark matter. Not surprisingly, we have also found that reasonable  $\Upsilon_{B,I}$  and  $\Upsilon_{D,I}$  values can describe the data well in 34 of our 40 galaxies; Figure 1(a) shows a good example (ESO 268g44). In some cases (*e.g.*, ESO 438g15 and ESO 502g02) the model predictions begin to drop below the data in the outer few points, but match the shape of the inner data.

The fit in the inner parts of eleven out of these 34 galaxies is significantly worse, due to bars and/or strong spirals that invalidate our assumption of circular orbits, but the amplitude and shape of the rotation curve over some radial range outside the barred region is predicted quite well by our mass model. Figure 1(b) shows an example of this behavior (ESO 439g20) – the model rotation curve runs significantly above the data values in the barred region, which is typical of these 11 cases.

Five of the remaining six cases exhibit the behavior seen for ESO 444g47 (Figure 1c), in which there is no significant radial range where the prediction matches the data. The predicted rotation curve shape begins to drop well before the optical edge, whereas the data do not; this shape difference is a clear indication of a mass discrepancy within the visible disk. With no dark matter component available, the fitting routine returns an unreasonably large  $\Upsilon_I$  in order that the underprediction farther out is balanced by a compensating overprediction of the observed speed in the inner parts. Since the  $\Upsilon_I$  is larger than can be allowed by the inner rotation curve in these five cases, we follow PW and eliminate the outer data to find the maximum allowable  $\Upsilon_I$ . Subsidiary fits in these five cases are also reported at the end of Table 2.

The remaining galaxy, ESO 381g05, shown in Figure 1(d), has large variations that are not well-predicted by the photometric model. This galaxy has a single strong spiral on one side, and may be disturbed by a recent, or on-going, merger.

The total stellar masses we derive agree quite well with those found by PW from the same data. The agreement is not perfect for several reasons: In all but five cases, our fits include all the kinematic data whereas PW limited their fits to the inner parts for all galaxies with outer mass discrepancies. Our disk-bulge decompositions are not identical and we also required  $\Upsilon_{B,I} > 0.5\Upsilon_{D,I}$  whereas PW frequently assigned much less mass to the bulge light. But the largest differences arise because we use kinematically defined inclination angles, whereas they preferred the inclination derived from the photometric image; in a few cases, this difference exceeds  $10^\circ$ , leading to quite substantial differences in  $\Upsilon_I$ . In fact, the largest discrepancy is for ESO 381g05, which may be tidally disturbed, calling the assumption of an intrinsic-

cally flat disk into question.

#### 4.1. Uncertainties

The uncertainty in the fitted  $\Upsilon_I$  values is due mostly to the uncertainties in the galaxy’s inclination, position angle, and distance. (Since we fit our models to a large number of data points, the  $\Upsilon_I$  values are tightly constrained once these parameters are fixed.) In a previous paper (Barnes & Sellwood 2003), we estimated systematic errors in inclination and position angles caused by spirals and other nonaxisymmetric structure in the galaxies. The best-fit value plus the estimated high and low limits for each of the two projection angles yield nine different combinations of inclination and position angle which give nine separate estimates for  $\Upsilon_I$  values. We take the uncertainty in an  $\Upsilon_I$  value to be half the range of these nine  $\Upsilon_I$  values.

Since  $\Upsilon$  is inversely proportional to distance, errors in our Hubble distances due to peculiar motions will also bias our estimated values. Indeed, this sample of galaxies was originally observed to study peculiar velocities in the region toward the “Great Attractor” and may therefore have larger than usual peculiar velocities. Since typical redshifts are 4000–5000 km/s, relative distance errors are unlikely to exceed 25%, however. Bothun *et al.* (1992) use the Tully-Fisher relation to estimate distances, finding differences between redshift distance and TF distance of typically about 25%. They find that the majority of these galaxies are actually closer than their Hubble distances, implying that our  $\Upsilon_I$  values may be underestimated by this factor.

#### 4.2. Discussion

For our sample, the average  $\Upsilon_{D,I}$  is 2.6 and the average  $\Upsilon_{B,I}$  is 2.8 (using the  $\Upsilon_I$  values of models with the best-fit  $i$  and  $\phi_0$ ). The average  $\Upsilon_{D,I}$  and  $\Upsilon_{B,I}$  systematic uncertainties are  $s_{\Upsilon_{D,I}} = 0.5$  and  $s_{\Upsilon_{B,I}} = 0.7$ .

Simulations by Bell & de Jong (2001) predict that the mass-to-light ratio of a stellar population should correlate with its intrinsic  $B-R$  color. Bell *et al.* (2003) have applied the Bell & de Jong models to a large sample of galaxies with multi-band photometry and find a somewhat shallower relation, with a large scatter, which we show by the

line in Figure 2(a). We plot our stars-only estimates of  $\Upsilon_{D,I}$ , but it should be noted that these dynamical estimates are only upper limits – the stellar  $\Upsilon_{D,I}$  could be lower if dark matter contributes significantly to the central attraction in the inner galaxy. The error bars on  $\Upsilon_{D,I}$  are the systematic uncertainties discussed above, and the arrows indicate how  $\Upsilon_{D,I}$  would change if the TF distance were used in place of the Hubble distance.

As we have only  $I$ -band images, we use galaxy colors obtained from the ESO-LV aperture magnitudes, as recorded in NED. In principle, we should compare the  $\Upsilon_{D,I}$  with the color of the disk alone, but NED gives magnitudes of the disk and bulge combined. The bulge light in our mostly late-type galaxies is a small fraction, typically  $\leq 10\%$ , of the total in the  $I$ -band, so any correction for the bulge to the total color is likely to be small. We have corrected the NED magnitudes for Galactic extinction using values from Schlegel, Finkbeiner & Davis (1998) and for internal extinction using the prescriptions of Tully *et al.* (1998). Errors in our estimated colors might be  $\sim 0.15$  mag.

Our average  $\Upsilon_{D,I}$  values (and those of PW) are in reasonable agreement with those found by Bell *et al.* (2003) and it is interesting that there are no points significantly below their trend. A point lying above the line, on the other hand, could simply indicate a significantly submaximal disk. While this could be the reason we see no trend, we first explore whether other effects could mask a trend in stars-only  $\Upsilon_{D,I}$  with color.

It is extremely unlikely that the corrections for the bulge light to the total colors could be large enough to destroy a trend, and the galaxies with no bulge (square symbols) also do not show one. Unfortunately, the number of galaxies without bulges is too small for a 2-D Kolmogorov-Smirnov test to determine whether this group is distributed differently from the bulge-and-disk galaxies in  $(\Upsilon_I, \text{color})$  space.

It is possible that a trend is masked by large errors in our  $\Upsilon_{D,I}$  values. The error bars include our estimate of the systematic error arising from uncertainties in the projection angles but do not include possible distance errors. They would have to be very large to mask the trend entirely, or conspire to correlate with color, which seems unlikely.

Bell *et al.* (2003) find the  $\Upsilon$  values of blue stellar



populations are more sensitive than red to metallicity. It is possible that the bluer galaxies in our sample are all metal-rich, but metallicity correlates with luminosity and we see no obvious trend of luminosity with color.

We are suprised not to see any trend of stars-only  $\Upsilon_{D,I}$  with color, since a trend has been seen in other work (*e.g.*, McGaugh 2004). The absence of a trend may imply that the halo contribution must correlate with color, which seems contrived for these bright HSB galaxies. The points in Figure 2(b) are encoded in many ways to distinguish galaxies by luminosity, field galaxies from those in clusters, the membership of different clusters, and the arrows show where the point would move if we adopted photometric inclinations, instead of kinematic. None of these appears to be a factor that could account for the absence of a trend.

## 5. Dark Matter Halo Fits

We next report fits to the velocity map that include a dark matter halo component. Since our adopted halo models have two free parameters, we now have to minimize  $\chi_b^2$  for either three or four parameters, depending on whether a separate  $\Upsilon_{B,I}$  is used.

Estimating statistical uncertainties from the  $\chi_b^2$  surface in a 4-parameter hypervolume is technically more difficult than for the 2-parameter stars-only models. The difficulty is compounded because we often find that the adopted halo parameters are strongly degenerate – that is, the minimum in the  $\chi_b^2$  hypersurface lies in a long, curved, and almost flat-bottomed valley. We estimate the uncertainties in each fitted parameter using a Markov Chain Monte Carlo method (*e.g.*, Christensen *et al.* 2001; Kosowsky, Milosavljević & Jimenez 2002), deriving the estimated likelihood of a set of parameters from the  $\chi_b^2$  value. Our Markov Chains for each galaxy contain 1 million elements and appear to be well-converged. We construct a histogram of the chain elements in the multi-dimensional parameter space; the likelihood region is the set of all bins with more than some threshold number of chain elements, with the threshold chosen such that the selected bins contain 68% of the chain elements. The set of chain elements in the selected likelihood region can then be projected onto the parameter axes to determine

the statistical uncertainties. Figure 3 shows an example for the Pseudo-isothermal (PI) halo model of ESO 322g82. Strictly speaking, these confidence regions are not exactly the 1- $\sigma$  uncertainties, since we define likelihoods from  $\chi_b^2$ , and not the usual  $\chi_r^2$  function. However, we find in practice that working with  $\chi_r^2$ , in cases where the outlying points have little effect on the position of the minimum, leads to very similar confidence regions.

We use an  $F$ -test to determine whether a halo is required to fit our data. This test determines whether the reduction in  $\chi_{b,\min}^2$  from the stars only case to when the fit includes the extra two halo parameters is large enough to justify the additional parameters. (Again, we treat  $\chi_b^2$  as an adequate surrogate for  $\chi_r^2$  and, of course, we always compare with  $\chi_r^2$  for the entire velocity map from the stars-only fits.) We discard the fits in a few cases only where this test indicates that there is less than 95% chance that the halo is necessary, since the values of the parameters in such cases are unlikely to be meaningful. Just three galaxies (ESO 317g41, ESO 382g06 & ESO 438g08) fail this test for all the types of halo we have fitted.

We also find in many cases that the halo drives  $\Upsilon_{D,I}$  to very low values, and the observed flow pattern is determined largely by the halo. It is clear that  $\Upsilon_{D,I} \ll 1$  is unphysical – the stellar population of the disk clearly must have some significant mass. Since the galaxies in our sample have quite normal colors, we regard  $\Upsilon_{D,I} < 0.5$  to be unrealistically low, and therefore discard any fits for which the 1- $\sigma$  upper bound on  $\Upsilon_{D,I} < 0.5$ . Very few cases fall just below this cut, and  $\Upsilon_{D,I} \ll 0.1$  for the large majority discarded for this reason. This criterion leads us to discard one galaxy in our sample (ESO 323g39) for all types of halo we have tried.

We have not attached any significance to the actual  $\chi_{b,\min}^2$  value, which always exceeds unity and is mostly greater than 2 – ranging up to greater than 11 in one case! Formally at least, large values of this parameter indicate that the model is an unacceptable fit to the data, which we do not dispute. However, examination of the residuals in the 2-D velocity map indicates that the large  $\chi_{b,\min}^2$  values arise from three principal sources: outlying points, bars, and spirals, in decreasing order of importance. We argue that large values of  $\chi_{b,\min}^2$  do not invalidate our estimates of halo parameters.

The biweight function is a robust statistic designed to minimize the influence of the outlying points, even though they still make a large contribution to the value of  $\chi_{b,\min}^2$  (eq. 6). The halo parameters are determined more by the overall shape of the rotation curve than by the non-axisymmetric streaming motions, which could possibly be modeled with a lot of effort (*e.g.* Weiner et al. 2001b), but do not affect the final parameter values to a great extent (Weiner *et al.* 2001a).

### 5.1. Pseudo-isothermal Halos

The PI density distribution is

$$\rho_{\text{PI}} = \frac{\rho_0}{1 + (r/r_c)^2}, \quad (7)$$

specified by two parameters  $\rho_0$ , the central density, and  $r_c$ , the core radius. The associated squared circular velocity is

$$v_{c,\text{PI}}^2 = v_\infty^2 \left[ 1 - \frac{r}{r_c} \arctan \left( \frac{r}{r_c} \right) \right], \quad (8)$$

where  $v_\infty \equiv (4\pi G\rho_0)^{1/2}r_c$  is the asymptotic circular velocity.

The best-fit parameters and their associated uncertainties for all 40 galaxies are given in Table 3. In only 3 cases out of the 40 galaxies in our sample does the addition of the extra two parameters for the halo lead to such a small reduction in  $\chi_{b,\min}^2$  that the halo is not needed; the value of  $\chi_{b,\min}^2$  in these cases is marked with an asterisk; we discard these three cases in the following discussion.

Ten of the remaining 37 galaxies have  $\Upsilon_{D,I}$  values for which the 1- $\sigma$  range never exceeds 0.5. Non-circular motions in the bar may be one of the factors that drives the solution towards a low  $\Upsilon_I$  value and a dominant halo. In these cases, the circular speed is often underestimated, while the rotation curve predicted by the luminous matter has a more steeply rising shape. Thus the fit can be improved by decreasing the  $\Upsilon_I$  and fitting the data mostly with the halo, which has a more adjustable shape. Whether this happens depends on other factors also, such as the bar orientation.

The halo parameters ( $\rho_0$  and  $r_c$ ) of the remaining 27 galaxies span a wide range, as shown in Figure 4. The line of slope  $-2$  in this plot is not a fit to the data, but shows the relation  $v_\infty^2 = 4\pi G\rho_0 r_c^2$

for  $v_\infty = 200$  km/s. Galaxies falling above (below) this line have larger (smaller) values of  $v_\infty$ . The fitted points are not randomly distributed about the line; the points above (below) the line tend to have large (small)  $r_c$  values. The distribution suggests, perhaps only marginally, that larger  $v_\infty$  galaxies, which also tend to be more luminous, have larger, lower-density cores than do the smaller galaxies. Despite using a slightly different cored dark matter distribution, the 6 galaxies presented in Gentile *et al.* (2004) follow essentially the same relation between central density and core radius. Donato, Gentile, & Salucci (2004) also present isothermal fits for 25 galaxies. Ten are “regular” spirals (neither dwarf nor low surface brightness), and they too lie among our points in the  $(\rho_0, r_c)$  plane. Donato, Gentile, & Salucci (2004) have additionally found a tight correlation between the disk scale length and  $r_c$ . PW fit exponential disks to their galaxies and determined disk scale lengths ( $R_d$ ), and we adopt these values as reasonable estimates. Despite the trend for the galaxies with larger  $v_\infty$ , and presumably larger disks, to have larger  $r_c$  values, we do not reproduce their claimed correlation between  $R_d$  and  $r_c$ . Kormendy & Freeman (2003) find  $\rho_0 \propto r_c^{-1.2}$  for PI halo fits, which is a shallower slope than the trend shown our Figure 4. However, their fits are made with the assumption of a maximum disk, which precludes central densities as high as some that emerge from our fits.

The three error bars that extend from points well beyond the right-hand edge are from three cases (ESO 322g45, ESO 323g73 & ESO 375g02) in which halo core radius is huge and very poorly constrained; the halo contribution to the circular speed rises essentially linearly to the outermost observed velocity. We are therefore unable to determine  $v_\infty$  with any confidence. Such degeneracy has been reported by other authors, even by Broeils (1992) who had high quality HI data extending to radii well outside the optical disk.

### 5.2. NFW Halos

The collapse of dark matter halos in simulations of large-scale structure formation yields halo density profiles that are not at all like the pseudo-isothermal function used above. The precise form of the density profile that emerges in these simulations is still disputed (Navarro, Frenk & White

1996; Power *et al.* 2003; Diemand, Moore & Stadel 2004), but all agree that the density increases steeply towards the center. We have therefore tried a broken power-law for the halo density profile. In this work, we treat the halo as spherical and make no attempt to take account of halo compression as a result of the cooling and settling of baryons to form the luminous component. Our objective is simply to assess whether the data are more consistent with a cusped density profile in galaxies today, and not to test detailed predictions from cold dark matter (CDM) simulations.

We adopt the original NFW density profile:

$$\rho_{\text{NFW}} = \frac{\rho_s r_s^3}{r(r+r_s)^2}, \quad (9)$$

where  $\rho_s$  is a scale density and  $r_s$  is a scale length. The squared circular velocity arising from this density profile is

$$v_{c,\text{NFW}}^2 = v_{200}^2 \left[ \left( \frac{c}{x} \right) \frac{\ln(1+x) - x/(1+x)}{\ln(1+c) - c/(1+c)} \right], \quad (10)$$

where  $x \equiv r/r_s$ ,  $c \equiv r_{200}/r_s$  is the concentration parameter and  $v_{200} = 10cr_s H_0$  is the circular speed at  $r_{200}$ . Inside the radius  $r_{200}$  the average density is 200 times the critical density of the universe ( $3H_0^2/8\pi G$ ).

The best-fit NFW parameters ( $c$  and  $v_{200}$ ) are listed in Table 4. The reduction in  $\chi_{b,\text{min}}^2$  is too small to justify the two halo parameters in 4 cases out of the 40 galaxies in our sample; the value of  $\chi_{b,\text{min}}^2$  in these cases is marked with an asterisk. Once again, we discard these for the remainder of this section. We also discard 16 of the remaining 36 galaxies because the  $1-\sigma$  range of their  $\Upsilon_{D,I}$  values never exceeds 0.5.

As with the pseudo-isothermal halo fits, the best fit NFW halo parameters of the remaining 20 galaxies have a considerable range, as shown in Figure 5. In only 9 cases, which tend to have higher values of  $c$ , the  $1-\sigma$  range of  $v_{200}$  does not extend up to values greatly in excess of any observed velocity. The enormous error bars for the other 11 galaxies indicate that the halo parameters are strongly degenerate. The line is the mean correlation between these halo parameters in a concordance  $\Lambda$ CDM simulation (Bullock *et al.* 2001). While our model halos are not directly comparable to those from simulations (see § 6.3 for a more

thorough discussion of the comparability of the simulated and model halos) and the uncertainties are quite large, the points in Figure 5 appear to describe a steeper trend than the prediction.

### 5.3. Power-law Halos

The results from fitting the above two standard halo models were not particularly informative for a number of reasons. Extreme minimum disks are often favored in a significant fraction of the galaxies (mostly those with strong non-axisymmetric features), which we then discard as unphysical. Also, the halo parameters are frequently highly degenerate since the minimum of the  $\chi_b^2$  hypersurface lies in a long, narrow, curved valley.

However, rotation curve data do tightly constrain something, namely the mass or mean density interior to the last measured point. The just-noted degeneracy in the NFW parameters arises because halos having the allowed wide range of parameters all have closely similar density profiles in the inner region that is the only part constrained by our data. Cases where no mass is assigned to the luminous material appear to arise because fitting functions with a length scale and a density scale as free parameters have too much freedom to adjust to quirks in our data.

We have therefore also tried a halo density profile with a smaller range of possible shapes: a single power law with no characteristic length scale. The density profile we adopt is

$$\rho_\alpha(r) = \rho_l \left( \frac{r_l}{r} \right)^\alpha, \quad (11)$$

where  $\rho_l$  is the halo density at  $r_l$ , the radius of our outermost velocity measurement. We stress that we fit this function only to the radial range spanned by our data and cannot say how the density profile continues beyond this radius. The squared circular velocity in this halo is

$$v_{c,\alpha}^2 = v_l^2 \left( \frac{r}{r_l} \right)^{2-\alpha}. \quad (12)$$

Again we have two free parameters,  $v_l$  and  $\alpha$ , with  $\rho_l = (3-\alpha)v_l^2/(4\pi G r_l^2)$ .

Table 5 gives the best-fit parameters and uncertainties for the power law fits. The reduction in  $\chi_{b,\text{min}}^2$  is too small to justify the two halo parameters in 6 out of the 40 galaxies in our sample; the

value of  $\chi_{b,\min}^2$  in these cases is marked with an asterisk. Once again, we discard these. We need to discard only 2 of the remaining 34 galaxies because the  $1\text{-}\sigma$  range of their  $\Upsilon_{D,I}$  values never exceeds 0.5. This small fraction contrasts with the 10 and 16 cases for the PI and NFW fits respectively.

With this halo form, we do not find strong degeneracies between the fitting parameters, implying that the fitted values are much more robust. Figure 6 shows that the halo parameters are also spread over a more limited range. Yet despite the more limited range of possible shapes, the values of  $\chi_{b,\min}^2$  are scarcely significantly larger than for the more flexible functions, and are actually smaller in a few cases.

The reason the power-law halo model is more useful, as judged by the preceding statistics, is that it has less flexibility. The length scale in the pseudo-isothermal and NFW halo models can produce a feature in the halo contribution that matches a feature in the data, thereby yielding a lower  $\chi_r^2$ , even though this is often achieved at the expense of driving  $\Upsilon_{D,I}$  to an absurdly low value. In these cases, it is likely that some non-axisymmetric disk feature drives the fit to this part of parameter space, rather than a true feature in the halo profile.

Figure 6 shows that the distribution of  $\alpha$  values is concentrated between  $0.8 \lesssim \alpha \lesssim 1.6$ , although a few values are close to zero and some range up to  $\alpha \lesssim 2$ . The significance of  $\alpha \gtrsim 1$  is unclear, however, since the probable halo contribution should be something in between uniform rotation and exactly constant orbital speed, which requires  $0 < \alpha < 2$ . While all intermediate values yield a halo rotation curve that rises fast initially and bends over to a less steeply rising part towards the outer radius, the abruptness of this transition does increase with  $\alpha$ , and the concentration of values in the range  $0.8 < \alpha < 1.6$  may be significant. Recent cosmological N-body simulations have also found similar  $\alpha$  values (Diemand, Moore & Stadel 2004).

## 6. Disk Masses and Halo Densities

### 6.1. Mass-to-light Ratios

We plot the  $\Upsilon_{D,I}$  values of the three halo models versus color in Figure 7. The error bars now reflect only the statistical uncertainties in  $\Upsilon_{D,I}$

values, and do not include any estimates of deprojection uncertainties which are of comparable magnitude, but which would be burdensome to compute. Since the colors are the same, the abscissae and their uncertainties in each panel are the same as in Figure 2. Each panel of this figure has fewer than 40 points because we have discarded any fit for which the halo was unnecessary or that yielded such a low  $\Upsilon_{D,I}$  value that its  $1\text{-}\sigma$  range never exceeded 0.5. We again indicate the relation fitted by Bell *et al.* (2003). The most striking feature of these plots is that adding halos has not changed the flat character of the distribution of points seen in Figure 2; we still do not see a trend with color for any of the three halo forms.

Our velocity data in a few cases do not require a halo component at all. This statement is true for all halo types in just three galaxies: ESO 317g41, ESO 382g06, and ESO 438g08. ESO 317g41 and ESO 438g08 have strong spirals, but ESO 382g06 is axisymmetric. The kinematic data for ESO 317g41 extends only to 80% of  $R_{23.5}$ , the radius at which the  $I$ -band surface brightness is  $23.5 \text{ mag/arcsec}^2$ . This raises the possibility that the radial extent of our data too small to probe the halo. However, for ESO 382g06 and ESO 438g08, the kinematic data extend at least to  $R_{23.5}$ , approximately 4 disk scale lengths. The rotation curves of these two galaxies turnover and decrease in the outer parts. As these galaxies appear to be baryon dominated, one might expect good agreement between our  $\Upsilon_{D,I}$  values and those predicted by Bell *et al.* (2003). In fact, we find that only ESO 438g08 is marginally consistent with the predicted value while the other two are several sigma above the prediction. Even though none of the simple halo functions tried here improves the fits by enough to justify the extra parameters, these three galaxies may yet have dark matters halos. In fact, if the halo rotation curve has a similar shape to that of the disk in the range covered by our data, any relative fraction would yield an equally acceptable fit.

Some galaxies, such as ESO 216g20 – the reddest in our sample, do seem to require a halo that makes their fitted  $\Upsilon_{D,I}$  fall below that expected for a stellar population of its color. We note that the TF-distance for this galaxy is larger than its Hubble distance, so its unusually low  $\Upsilon_{D,I}$  is unlikely to result from too short an adopted distance.

ESO 322g44 is another case which falls below the line in all three panels and there are others which are low when we accept the fit, and are discarded as unrealistically low for other halo types.

Of the galaxies lying above the line from Bell *et al.* (2003) in Figure 2, only one of the bluest galaxies in our sample, ESO 446g01, remains significantly above the line in all the  $\Upsilon_I$  vs. color plots, while three other galaxies (ESO 381g05, ESO 437g31, ESO 501g01) lie well above the line for the type(s) of halo(s) for which we accepted the fit, but are discarded for other types. The introduction of any of three halo types into these four galaxies did not reduce their  $\Upsilon_{D,I}$  values to the predicted value.

None of our adopted halo models yields  $\Upsilon_{D,I}$  values that follow the trend found by Bell *et al.* (2003). It is possible that systematic errors such as distance and/or inclination errors, radial extinction variations, gas mass corrections, thickness corrections, non-circular motions, etc., have masked the expected trend, but they would have to be as large as factors of three, and in a sense to correlate with color. It is more likely that our models have mis-estimated the dark matter content in the majority of these galaxies, and our  $\Upsilon_{D,I}$  values are spurious.

Figure 8 compares the  $\Upsilon_{D,I}$  values obtained from each of our fits to the 2-D velocity maps. Each panel displays considerable scatter. The values from adopting one halo model are frequently inconsistent with those from another model at the several- $\sigma$  level, although a few cases, which generally have smaller uncertainties, do lie nicely on the diagonals in all three panels. The open circles mark galaxies which fail the  $F$ -test for either of the halo models. The most significant feature in this Figure is that the NFW halo density profile generally leads to the lowest assigned  $\Upsilon_{D,I}$  value of the three functions we have tried.

## 6.2. Halo Masses

We have determined the total mass in the halo interior to our outermost available velocity measurement. The halo masses for the three different functional forms, normalized by total enclosed mass, are compared in Figure 9. Again, the open circles mark galaxies which fail the  $F$ -test for either of the halo models. We have used our MCMC

study to determine the confidence intervals, which range up to 70% in the worst few cases but are generally much lower.

It is clear from this Figure that the NFW form tends to require a larger halo mass fraction than the other two types, which is consistent with its generally lower disk masses. Many cases require no halo or negligible disk mass, and other cases show large differences in fitted halo masses between the different halo models.

In general, the agreement between the halo masses calculated for the different halo types is poor. For 12 galaxies, the total uncertainty in PI halo mass fraction is  $< 0.2$ . These galaxies are, on average,  $2.3\sigma$  away from agreeing with the NFW halo mass fractions and are  $2.1\sigma$  away from agreeing with the power-law halo mass fractions. The 5 galaxies which have NFW halo mass fraction uncertainties  $< 0.2$  are  $1.3\sigma$  and  $2.1\sigma$  from agreeing with the PI and power-law values, respectively. Finally, 17 galaxies have power-law halo mass fraction uncertainties  $< 0.2$ . These galaxies are  $2.2\sigma$  and  $2.3\sigma$  away from agreeing with the PI and NFW values, respectively. However, in a few cases the halo mass fraction has a small uncertainty, is neither 0 nor 1, and lies close to the diagonal in this Fig. 9. One such case is ESO 445g15, for which we claim a consistent and well-constrained halo mass fraction for all three density profiles we tried.

Aside from these rare cases, we conclude that not even our 2-D data constrain the dark matter content of a galaxy – the fitted amount is either highly uncertain, or depends on the halo mass function adopted.

## 6.3. Halo Densities

Cosmological simulations make predictions for the central densities of dark matter halos. Specifically, Alam, Bullock & Weinberg (2002) introduce a measure of the central densities of halos,  $\Delta_{v/2}$ , which is the average halo density inside the radius at which the velocity is half the maximum halo velocity [ $\rho(R_{v_h/2})$ ], normalized by the critical density of the universe,  $\rho_c = 3H_0^2/(8\pi G)$ . Their Figure 2 plots the predicted  $\Delta_{v/2}$  from an  $\Lambda$ CDM simulation versus maximum halo velocity  $v_{\max}$  in which larger dark matter halos (high  $v_{\max}$ ) have lower densities. The same figure has points de-

rived from real galaxies which do not appear to follow the predicted trend.

We show our derived  $\Delta_{v/2}$  versus  $v_{\max}$  for the NFW halos only in Figure 10. The line illustrates the trend expected from simulations (Zentner & Bullock 2002). One point marked by an open circle is one of the four cases for which the  $F$ -test indicates no halo is required, two other cases are points off the left side of the plot, and the fourth case cannot be plotted as the best fit assigns zero halo mass. The points without symbols, which lie mostly above the line, are fits with very low  $\Upsilon_{D,I}$ . The rest are marked with filled symbols. Those that have enormous error bars are cases that are degenerate, because our optical data do not extend far enough to constrain  $r_s$ .

Our data points are not directly comparable with predictions of  $\Lambda$ CDM, since the simulated halos should be compressed by baryonic infall. To make a detailed test, we should include halo compression as a step in the minimization loop in order to determine the parameters of the uncompressed halos, possibly also testing a range of uncompressed density profiles as part of the uncertainty in the predictions. Our less ambitious approach is simply to test whether the NFW profile describes galaxy halos in the local universe any more closely than the others. Thus our parameters, if they have any relevance at all, are for compressed halos. It is clear that the mean densities of the uncompressed halos would be lower, by an amount that depends on the stellar mass.

The large error bars on many points make it difficult to conclude much from this Figure; we cannot claim that our data are inconsistent with the prediction, but neither do they offer much support for it. This result is similar to the outcomes in other studies that compare simulations to parameters derived from galaxies (Alam, Bullock & Weinberg 2002; Zentner & Bullock 2002). Even points with small error bars have a large scatter about the line, whereas the simulations predict a rms scatter of about a factor 3 (Alam, Bullock & Weinberg 2002). We also note that as points without symbols represent fits that attribute essentially no mass to the luminous matter, more realistic fits would attribute a lower average halo density and move those points to lower  $\Delta_{v/2}$  values.

We cannot make a similar plot for the power

law halo, since we know nothing about how the profile may vary at radii beyond our data. However, we did obtain the lowest halo mass with this function (Fig. 9) which, combined with the greater compression from the more massive disks suggests that the densities are considerably lower than for the NFW halos.

## 7. Rotation Curve Fitting

In this section we compare our results from the 2-D velocity maps with what could be achieved for the same galaxies from 1-D longslit data. As we do not have separate longslit data, we extract pseudo-data from the 2-D velocity map along a line across the major axis of the galaxy.

### 7.1. Pseudo-slit Rotation Curves

We mimic data that could result from longslit spectroscopy, by placing a “slit” along the photometric major axis of each galaxy and passing through the point of brightest continuum emission. We extract the mean velocity,  $v_{\text{los}}$ , and its uncertainty from our 2-D velocity maps every  $1.5''$ , a typical seeing length, from the pixel whose center is closest to the chosen line; interpolation or averaging over several pixels is unnecessary, since the pixel sizes are generally less than the seeing. The S/N in any one pixel of our map is probably less than would be obtained from a longslit observation, but not by a large factor. (The FP scan used 10 min exposures at each filter setting, but as the device used has about twice the throughput of a typical spectrograph, our S/N may be equivalent to that from a 20 min spectrographic observation.)

We treat these data by the typical procedures for longslit data (*e.g.*, de Blok, McGaugh & Rubin 2001). We estimate the systemic velocity by folding the  $v_{\text{los}}$  curve, by eye, assuming that the receding and approaching sides are symmetric.

Since a velocity map allows us to determine  $v_s$  with greater precision, we have investigated the differences between the  $v_{s,\text{map}}$  and  $v_{s,\text{slit}}$  values. The rms difference between the systemic velocities derived from the pseudo-slit data and our velocity maps is  $\Delta_{\text{sys}} = 10$  km/s. It is interesting to break this comparison down for axisymmetric, spiral, and barred galaxies. Axisymmetric galaxies (disks without strong spiral structure) have  $\Delta_{\text{sys}} = 6$  km/s. Galaxies with spirals have

$\Delta_{\text{sys}} = 13$  km/s. Overall, barred galaxies have  $\Delta_{\text{sys}} = 10$  km/s. We further subdivide the barred galaxies according to the position angle of the bar. When the bar lies along the minor axis,  $\Delta_{\text{sys}} = 8$  km/s. Galaxies with bars at an oblique angle to the major axis have  $\Delta_{\text{sys}} = 12$  km/s and those with major axis bars have  $\Delta_{\text{sys}} = 10$  km/s. In the central regions of these galaxies where typically the rotation curves rise approximately linearly, the uncertainty in  $v_{s,\text{slit}}$  relates directly to an uncertainty in the position adopted for the center. Using the maximum uncertainty quoted above leads to an uncertainty in dynamical center positions  $\lesssim 1''$ .

We retain all the points (receding and approaching) as independent data points in the rotation curves. Finally, we correct the rotation speeds for inclination using the photometric value since this is all slit observers would have at their disposal.

## 7.2. Comparison of Map and Pseudo-slit Rotation Curves

Our pseudo-slit rotation curves generally agree well with those we derived from the 2-D velocity maps. A few illustrative cases are shown in Figure 11; the dotted error bars denote pseudo-slit data, while the solid points are from our fits to the 2-D maps. Panel (a) shows an example (ESO 322g82) of good agreement between the two curves. The case in panel (b) shows a galaxy with strong spirals (ESO 322g36); velocities differ between the approaching and receding sides over the radial range from 3 to 8 kpc, but the velocity map rotation curve nicely bisects this asymmetry. The agreement between the two curves in panel (c) (ESO 438g08) is poor, which results from a disagreement between the photometric major axis that a slit observer would use and the major axis that we find from our 2-D velocity map; the spirals present in this galaxy have biased the estimate of photometric position angle (see Barnes & Sellwood (2003) for a fuller discussion of this effect). The case shown in panel (d), ESO 501g01, shows the greatest advantage of velocity map data over slit spectroscopy, since this galaxy has major axis H $\alpha$  emission over only a limited radial range, whereas the velocity map allows a much greater radial range to be explored.

## 7.3. Mass Models

We have used our pseudo-slit rotation curves to determine  $\Upsilon_I$  values in a manner similar to the 2-D data. We fit constant  $\Upsilon_I$  models, to the inclination-corrected velocities, using the same procedure as described above, but for this much smaller number of pixels. As before, we first fit models without halos and then include the three different halo types.

### 7.3.1. Stars-only Fits

The comparison of pseudo-slit and map  $\Upsilon_I$  values is illustrated in Figure 12. The pseudo-slit and map  $\Upsilon_{D,I}$  values have rms fractional differences of 22% while the  $\Upsilon_{B,I}$  values differ by 39%. We find that in 28 of 40 galaxies the pseudo-slit  $\Upsilon_{D,I}$  values are 25% lower than the map  $\Upsilon_{D,I}$  values. The remaining 12 galaxies have map  $\Upsilon_{D,I}$  values which are 13% less than the pseudo-slit values. In 17 of the 31 galaxies with bulges, the pseudo-slit  $\Upsilon_{B,I}$  values are 30% lower than the map  $\Upsilon_{B,I}$  values. The other 14 galaxies have map  $\Upsilon_{B,I}$  values 49% smaller than the pseudo-slit values. A few outliers inflate these averages, so the overall  $\Upsilon_{D,I}$  differences are closer to 15% and the  $\Upsilon_{B,I}$  differences are more like 25%. Three of the worst outliers in the  $\Upsilon_{D,I}$  comparison (ESO 381g05, ESO 382g06, ESO 445g39) have quite poor agreement between the pseudo-slit and velocity map rotation curves. Two others (ESO 323g39 and ESO 438g08) have slit misalignment issues. However, the trend for pseudo-slit  $\Upsilon_{D,I}$  values to be lower than the map  $\Upsilon_{D,I}$  values remains.

This trend may have an explanation in the differing methods. Fitting pseudo-slit data gives equal weight to each data point regardless of radial location. However, velocity map fits utilize more data as radius increases, giving more weight to the outer regions of the rotation curves. Since the outermost points tend to have higher velocity, the map  $\Upsilon_{D,I}$  values reflect this by being slightly larger. We find a similar bias when halos are added – see below.

As expected for fewer data points, the average pseudo-slit statistical uncertainties are  $\approx 3$  times larger than the velocity map statistical uncertainties. The systematic uncertainties due to position angle uncertainties are of the same magnitude for both methods, and the estimated systematic error

in  $\Upsilon_I \approx 0.5$ . As with the stars-only map fits, the  $\Upsilon_I$  values do not show any trend with color.

### 7.3.2. Halo Fits

As with the 2-D velocity maps, we have fitted the three halo models to these rotation curves from 1-D pseudo-slit data. Figure 13 shows how the halo mass fraction (within the radius of the outermost fitted point from the velocity map) compares between the fits to the pseudo-slit data and the velocity maps.

Not surprisingly, we find constraints on the halo masses are generally weaker for slit data than for 2-D maps, by a factor  $\gtrsim 2$  in most cases. The significant outliers in these plots are generally cases of disagreement between the photometric inclination adopted for the pseudo-slit, and the kinematic inclination used for the velocity map.

The slit-estimated halo masses tend to be higher than the map-estimated values, which we attribute to the above-noted significance of the large number of pixels in the outer parts of the map. Since slit data give greater relative weight to the inner points, an overfit in the inner parts carries a greater penalty, sometimes forcing  $\Upsilon_{D,I}$  to lower values, which requires more halo mass to match the outer data.

## 8. Summary & Conclusions

Palunas & Williams (2000) present a sample of homogeneously collected, 2-D optical velocity maps and *I*-band surface brightness distributions of galaxies. We have re-analyzed a subsample of these galaxies, omitting mostly those that are highly inclined, in order to determine whether such data constrain the dark matter content of these galaxies any more tightly than do previous studies using longslit data or velocity maps at lower spatial resolution.

Our results echo those of PW in finding that the stars-only model fits the shape of the observed rotation curve over a significant radial range in 34 out of the 40 cases. This fraction includes 11 cases where bars or spirals cause a mismatch in the inner barred region which we argue is acceptable because of non-circular motion. A further 5 cases could be fitted tolerably well when the outer data were discarded, as found by PW. In addition to these 5 galaxies, several others have noticeable

mass discrepancies in the outer parts. These stars-only fits yield an average  $\Upsilon_{D,I}$  of 2.6 and an average  $\Upsilon_{B,I}$  of 2.8, similar to the values found by PW. The main sources of uncertainty in these estimates are those arising from distance errors and possible errors in the adopted projection geometry.

These average  $\Upsilon_I$  values, even with no dark matter, are in the range predicted from stellar population models, but we do not find a trend of  $\Upsilon_I$  with color. Instead of finding lower  $\Upsilon_I$  values for bluer galaxies, we find a flat distribution which does not decrease for the bluest galaxies.

We fitted three dark matter halo profiles; two are standard, pseudo-isothermal (PI) and Navarro-Frenk-White (NFW), and we have also used a simple power law function over the radial range of our data. Three galaxies in our sample do not require a halo of any type we tried, although these galaxies may have dark matter halos of some other form. Should the true inner halo rotation curve shape resemble that of the luminous matter, any relative fraction would yield an equally acceptable fit; studies such as this, which are based on rotation curve data alone, could never break such a degeneracy.

In most cases, the fit to the data is significantly improved by adding one or more of our adopted halos, but we do not find a preference for any particular halo density profile, in the sense that the values of  $\chi_{b,\min}^2$  are all rather similar no matter which form is adopted. However, we find wide variations in the  $\Upsilon_{D,I}$  values and halo masses, within the radial range spanned by our data, depending upon which halo density profile is adopted. This finding implies that even with high-quality 2-D data, rotation curve fitting is unable to determine either the disk mass-to-light ratio, halo mass, or density profile with any degree of confidence.

The pseudo-isothermal and NFW halo models, which have both a length scale and a density normalization as free parameters, often lead to fitted  $\Upsilon_I$  values that are absurdly low, which seems to indicate that such functions have too much freedom to adjust their shapes to quirks in the velocity maps, such as may arise from non-axisymmetric features in the disk. These functional forms also lead to strong degeneracies in the fitted parameters, especially for low halo densities. Our suggested power-law halo density profile is more ro-



bust, in the sense that it does not have strong degeneracies and requires fewer near-massless stellar populations.

Following the suggestion of Alam, Bullock & Weinberg (2002), we have calculated the central density parameter  $\Delta_{v/2}$  for the fitted NFW halos. We find that our fitted halo densities are highly uncertain, but seem to span a very wide range that includes values consistent with the predictions from cosmological simulations but also extend to much lower densities; a few galaxies have no detectable dark matter at all.

Fits with the NFW halo function generally attribute the least mass to the disk, and the most to the halo, while the power law prefers the highest disk masses. On average, the power-law halos have radial density profiles  $\propto r^{-1}$  or somewhat steeper, *i.e.* a slope resembling the inner parts of halo density profiles from recent cosmological simulations of structure formation (Diemand, Moore & Stadel 2004). However, the corresponding mean halo densities are generally lower than those obtained with the NFW function.

We have compared our fitted  $\Upsilon_{D,I}$  values with population synthesis models. While our stars-only  $\Upsilon_{D,I}$  values (Fig. 2) are in the range predicted by Bell *et al.* (2003), we do not find a trend with color. When halos are included (Fig. 7), many  $\Upsilon_{D,I}$  values are lower than their predictions. Distance errors affect the estimated  $\Upsilon_I$  directly, but it is unlikely they could be large enough to bring the points into agreement with the prediction; frequently, adopting Tully-Fisher distances instead of Hubble distances would reduce  $\Upsilon_{D,I}$  still further. Also, we do not see a correlation between color and distance, luminosity (metallicity), or cluster membership needed to recover the predicted trend. The most likely explanation is that none of our models has captured the actual distribution of dark matter in our sample of galaxies and, without this knowledge, our fits cannot determine the true  $\Upsilon_{D,I}$ .

We have compared our results from fitting 2-D velocity maps with those from pseudo-slit data extracted from our data on the photometric major axis only. Derived rotation curves generally agree reasonably well with the rotation curves from the velocity maps. In a few cases, disagreement stems from misaligned slits, poor major axis data, and/or nonaxisymmetric structure.

Not surprisingly, we find the uncertainties in the estimated parameters are  $\approx 3$  times larger from pseudo-slit data than from the 2-D maps. We find a tendency for  $\Upsilon_I$  values from our pseudo-slit data to be  $\approx 15\%$  lower than the corresponding velocity map values, which we attribute to the extra weight that 2-D maps give to the larger number of data values in the outer parts of the map. The greatest improvements afforded by 2-D velocity maps is that they offer tighter constraints on the projection geometry and the systemic velocity, as well as revealing more extensive rotation curves in cases with sparse data along their major axes.

Fits of axisymmetric models to two-dimensional velocity maps, even at optical resolution, do not provide significant constraints on either the mass-to-light of the luminous matter or the halo mass fraction or its density profile. Additional data extending to larger radii, *e.g.* from neutral hydrogen maps, must tighten the constraints somewhat, but the improvement is not dramatic; *e.g.* Blais-Ouellette, Amram & Carignan (2001) still find large variations in  $\Upsilon_{D,I}$  and halo mass between the different halo models. We therefore conclude that additional information is needed to constrain the disk mass, and therefore also the halo density, in a galaxy.

The authors gratefully acknowledge the assistance and advice of Povilas Palunas, Ted Williams, Tad Pryor, and Stacy McGaugh. We thank Eric Peng, Pat Côté, and Laura Ferrarese for a number of helpful discussions. We also acknowledge James Bullock for supplying us with the cosmological simulation results shown in Figures 5 and 10. An anonymous referee supplied a detailed report based on a very careful read that helped us to improve the paper. This work has been supported by NASA grant NAG 5-10110. AK is a Cottrell Scholar of the Research Corporation.

## REFERENCES

- Alam, S. M. K., Bullock, J. S., Weinberg, D. H. 2002, *ApJ*, 572, 34
- van Albada, T. S., Bahcall, J. N., Begeman, K., Sancisi, R. 1985, *ApJ*, 295, 305
- Andersen, D. R., Bershad, M. A. 2002, *BAAS*, 34, 1219
- Arimoto, N., Yoshii, Y. 1986, *A&A*, 164, 260
- Balcells, M., Graham, A. W., Domínguez-Palmero, L., Peletier, R. F. 2003, *ApJ*, 582, L79
- Barnes, E. I., Sellwood, J. A. 2003, *AJ*, 125, 1164
- Bell, E. F., de Jong, R. S. 2001, *ApJ*, 550, 212
- Bell, E. F., McIntosh, D. H., Katz, N., Weinberg, M. D. 2003, *ApJS*, 149, 289
- Binney, J., Tremaine, S. 1987, *Galactic Dynamics*, Princeton Univ. Press, Princeton
- Blais-Ouellette, S., Amram, P., Carignan, C. 2001, *AJ*, 121, 1952
- Bosma, A., van der Hulst, J. M., Sullivan, W. T. 1977, *A&A*, 57, 373
- Bothun, G. D., Schommer, R. A., Williams, T. B., Mould, J. R., Huchra, J. P. 1992, *ApJ*, 388, 253
- Bottema, R. 1997, *A&A*, 328, 517
- Broeils, A. H. 1992, PhD Thesis, University of Groningen
- Bruzual, G. A., Charlot, S. 1993, *ApJ*, 95, 107
- Bullock, J. S., Kolatt, T. S., Sigad, Y., Somerville, R. S., Kravtsov, A. V., Klypin, A. A., Primack, J. R., Dekel, A. 2001, *MNRAS*, 321, 559
- Christensen, N., Meyer, R., Knox, L., Luey, B. 2001, *Classical and Quantum Gravity*, 18, 2677
- Corradi, R. L. M., Boulesteix, J., Bosma, A., Amram, P., Capaccioli, M., 1991, *A&A*, 244, 27
- Courteau, S. 1997, *AJ*, 114, 2402
- Davies, R. L., Kuntschner, H., Emsellem, E., Bacon, R., Bureau, M., Carollo, C. M., Copin, Y., Miller, B. W., Monnet, G., Peletier, R. F., Verolme, E. K., de Zeeuw, P. T. 2001, *ApJ*, 548, L33
- de Blok, W. J. G., McGaugh, S. S., Rubin, V. C. 2001, *AJ*, 122, 2396
- de Vaucouleurs, G., de Vaucouleurs, A., Corwin, H. G., Jr., Buta, R. J., Paturel, G., Fouqué, P. 1991, *Third Reference Catalogue of Bright Galaxies* (New York: Springer) (RC3)
- Diemand, J., Moore, B., Stadel, J. *astro-ph/0402267*
- Donato, F., Gentile, G., Salucci, P. 2004, *MNRAS*, 346
- Gentile, G., Salucci, P., Klein, U., Vergani, D., Kalberla, P. 2004, *astro-ph/0403154*
- Jimenez, R., Verde, L., Oh, S. P., *MNRAS*, 339, 243
- Jogee, S., Knapen, J. H., Laine, S., Shlosman, I., Scoville, N. Z., Englmaier, P. 2002, *ApJ*, 570, L55
- de Jong, R. S. 1996, *A&A*, 313, 377
- Kranz, T., Slyz, A., Rix, H.-W. 2003, *ApJ*, 586, 143
- Kormendy, J., Freeman, K. 2003, in *IAU Symp. 220, Dark Matter in Galaxies*, ed. S. Ryder, D. J. Pisano, M. Walker, & K. (Dordrecht: Reidel), 377
- Kosowsky, A., Milosavljevic, M., Jimenez, R. 2002, *Phys. Rev. D*, 66, 063007
- Lake, G., Feinswog, L. 1989, *AJ*, 98, 166
- McGaugh, S. S. 2004, *ApJ*, 609, 652
- Navarro, J. F., Frenk, C. S., White, S. D. M. 1996, *ApJ*, 462, 563
- Navarro, J. F. 1998, *astro-ph/9807084*
- Palunas, P., Williams, T. B. 2000, *AJ*, 120, 2884 (PW)
- Power, C., Navarro, J. F., Jenkins, A., Frenk, C. S., White, S. D. M. 2003, *MNRAS*, 338, 14
- Press, W. H., Flannery, B. P., Teukolsky, S. A., Vetterling, T. A. 1992, *Numerical Recipes* (Cambridge: Cambridge Univ. Press)

- Regan, M. W., Thornley, M. D., Helfer, T. T., Sheth, K., Wong, T., Vogel, S. N., Blitz, L., Bock, D. C.-J. 2001, *ApJ*, 561, 218
- Schlegel, D. J., Finkbeiner, D. P., Davis, M. 1998, *ApJ*, 500,525
- Sérsic, J.-L. 1968, Atlas de galaxias australes, Observatorio Astronomico, Cordoba
- Simon, J. D., Bolatto, A. D., Leroy, A., Blitz, L. 2003, *ApJ*, 596, 957
- Sofue, Y., Rubin, V. 2001, *ARA&A*, 39, 137
- Sofue, Y., Koda, J., Nakanishi, H., Onodera, S. 2003, *PASJ*, 55, 59
- Stark, A. 1977, *ApJ*, 213, 368
- Tully, R. B., Pierce, M. J., Huang, J., Saunders, W., Verheijen, M. A. W., Witchalls, P. L. 1998, *AJ*, 115, 2264
- van den Bosch, F. C., Robertson, B. E., Dalcanton, J. J., de Blok, W. J. G. 2000, *AJ*, 119, 1579
- Verheijen, M. A. W. 1997, PhD Thesis, University of Groningen
- Verheijen, M. A. W., Bershady, M., Andersen, D., Swaters, R., Westfall, K., Kelz, A., Roth, M-M. 2003, astro-ph/0311555
- Vogt, N. P., Haynes, M. P., Herter, T., Giovanelli, R. astro-ph/0402649
- Weiner, B. J., Williams, T. B., van Gorkom, J., Sellwood, J. A. 2001, *ApJ*, 546, 916
- Weiner, B. J., Sellwood, J. A., Williams, T. B. 2001, *ApJ*, 546, 931
- Weiner, B. J. 2003, in IAU Symp. 220, Dark Matter in Galaxies, ed. S. Ryder, D. J. Pisano, M. Walker, & K. Freeman (Dordrecht: Reidel), 35
- Worthey, G. 1994, *ApJS*, 95, 107
- Zentner, A. R., Bullock J. S. 2002, *Phys. Rev. D*, 66, 043003

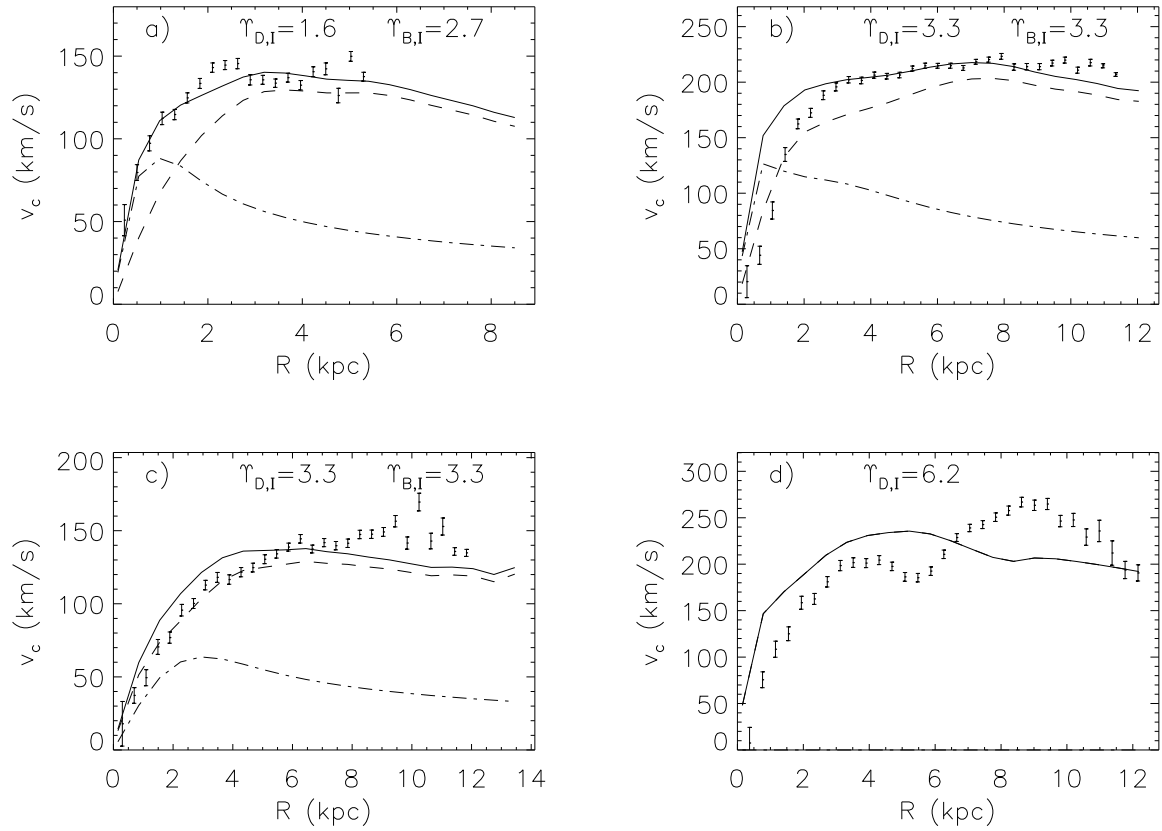


Fig. 1.— Various types of rotation curves for the stars-only models. The dashed line represents the disk contribution. The bulge contribution is shown with the dash-dotted line. The solid line is the combination disk+bulge. a) ESO 268g44: an example of good agreement between model and data. b) ESO 439g20: a barred galaxy for which the model overpredicts the inner rotation curve; the bar has a half-length of approximately 2 kpc. c) ESO 444g47: an example of an overfitted disk driven by an evident mass discrepancy in the outer regions. d) ESO 381g05: a galaxy with strong spirals and a possible tidal distortion.

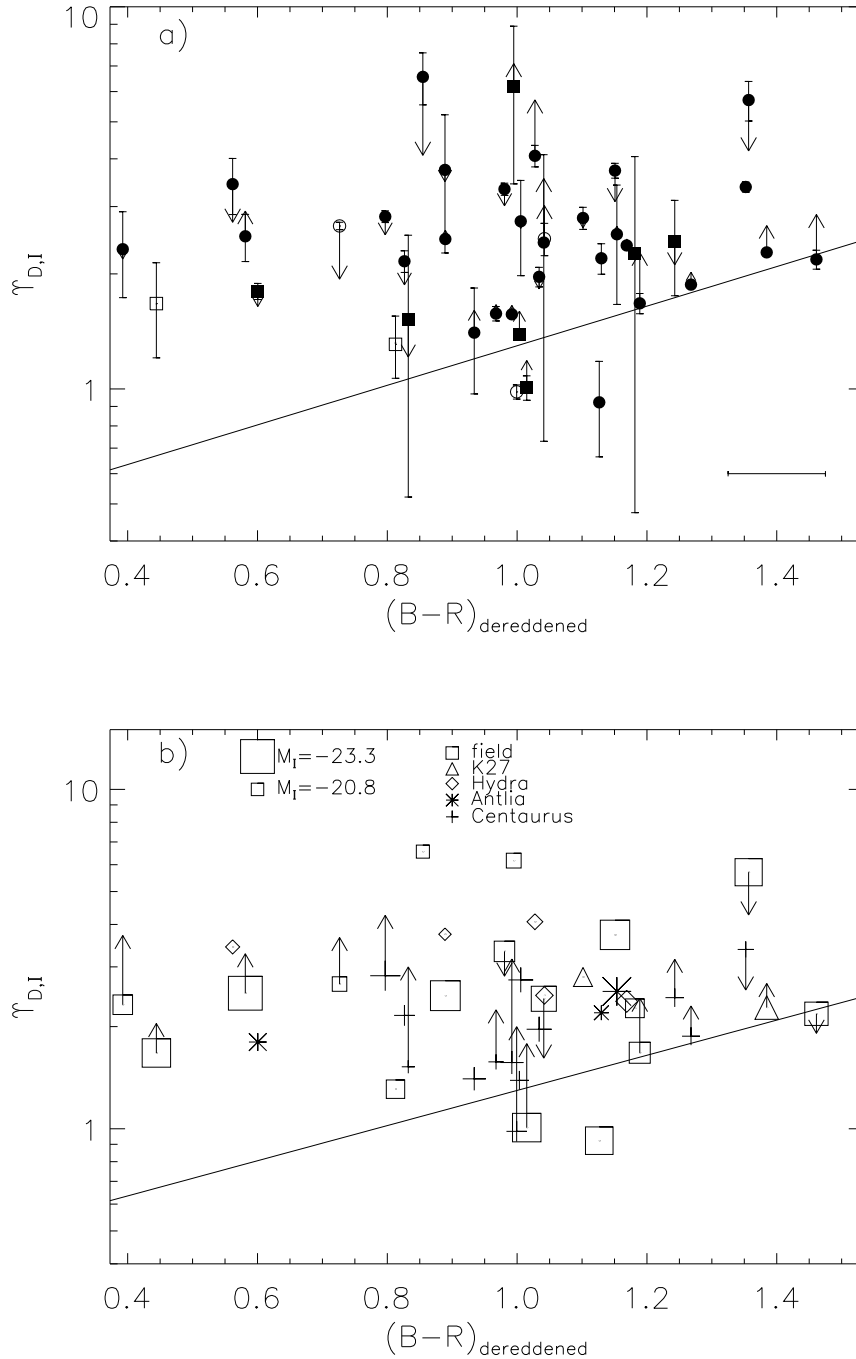


Fig. 2.— Fitted  $\Upsilon_{D,I}$  values for stars-only vs. dereddened  $B - R$ . In both panels the line is the best-fit correlation found by Bell *et al.* (2003). (a) Estimated systematic errors are shown and the arrows indicate how the points would move were the photometric inclinations used to derive  $\Upsilon_{D,I}$  values. Squares denote galaxies without bulges. Galaxies with evidence of mass discrepancies are marked by open symbols, and their  $\Upsilon_{D,I}$  values are the maximum-disk values from Table 2. The horizontal errorbar in the lower right corner indicates the estimated error in the color adopted for each galaxy. (b) The same plot, but the different symbols denote whether a galaxy belongs to a cluster or the field. Larger symbol sizes correspond to more luminous (and more metal rich) galaxies. The arrows show how points would move if their Tully-Fisher distances were used instead of Hubble distances.

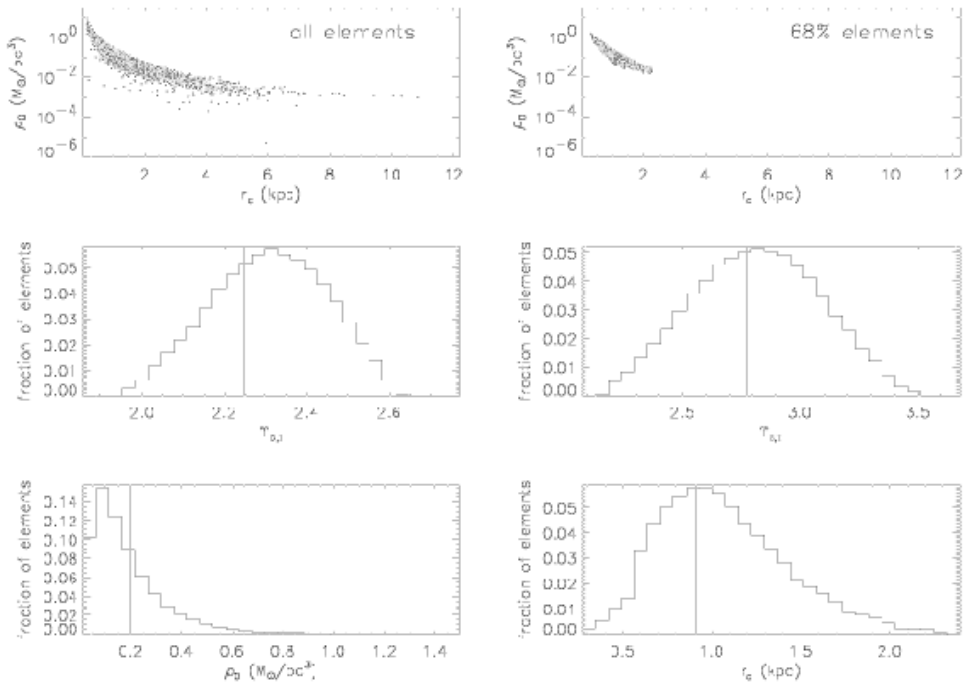


Fig. 3.— Top left shows the projection of all Markov Chain Monte Carlo elements onto the  $\rho_0$ - $v_\infty$  plane for the PI halo fit to ESO 322g82, to illustrate the strong degeneracy of these parameters. (Only 1 point in 300 is plotted.) Top right shows the same projection of the 68% of points lying in the densest part of the parameter hypervolume. The other four panels show histograms of the same 68% of selected points projected onto the four parameter axes. The vertical line in each panel shows the best fit value.

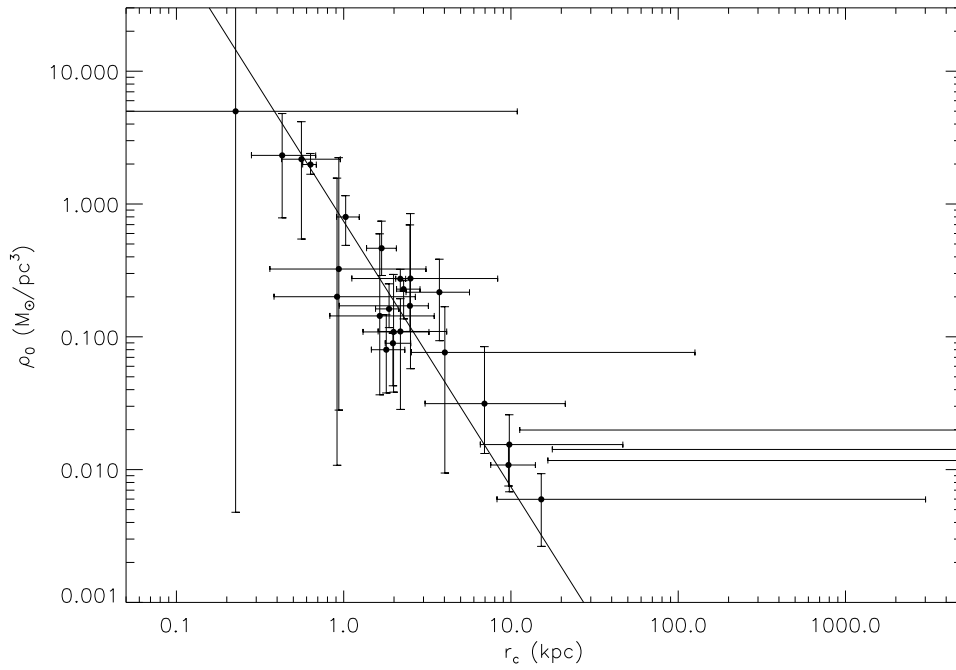


Fig. 4.— Central density versus scale radius for the PI fits. The solid line is not a fit to the points, but shows the relation between the parameters for  $v_\infty = 200$  km/s. Note a marginal tendency for the halos with higher central densities to fall below the line while lower density halos lie above it.

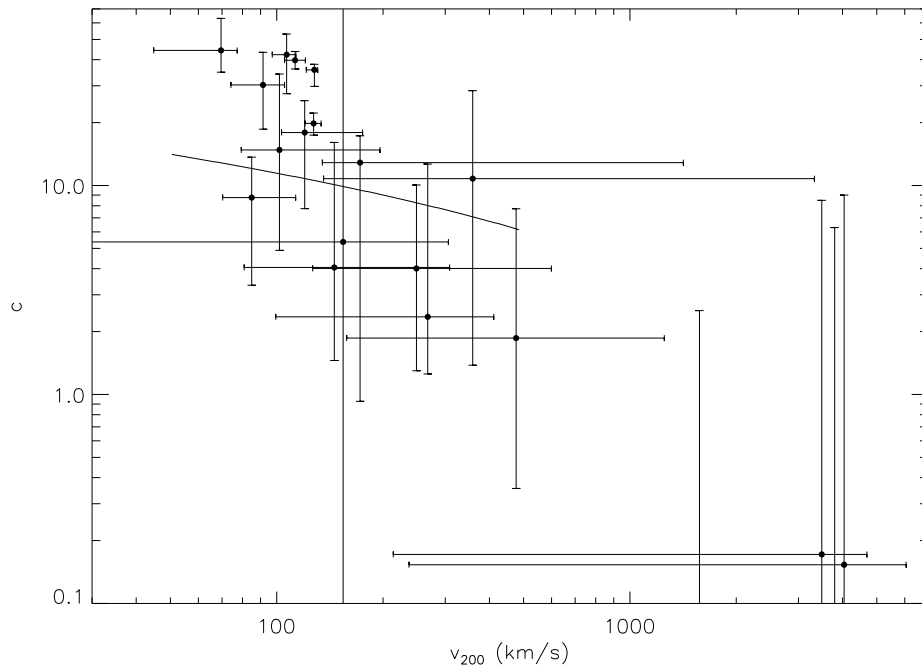


Fig. 5.— Concentration versus  $v_{200}$  for the NFW fits. Note how the uncertainties rapidly increase as the halos become less dense and more extended. The solid line illustrates the mean correlation found in the simulation of Bullock *et al.* (2001).



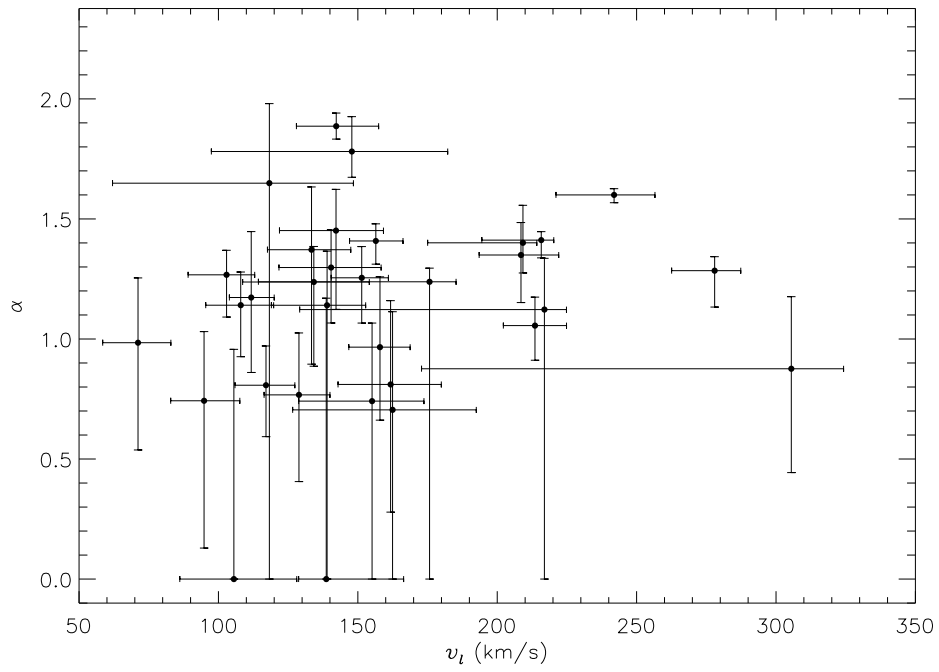


Fig. 6.— Slope parameter  $\alpha$  versus  $v_l$  for the power-law fits. The  $\alpha$  values have an average value of 1.1, but have a wide range.

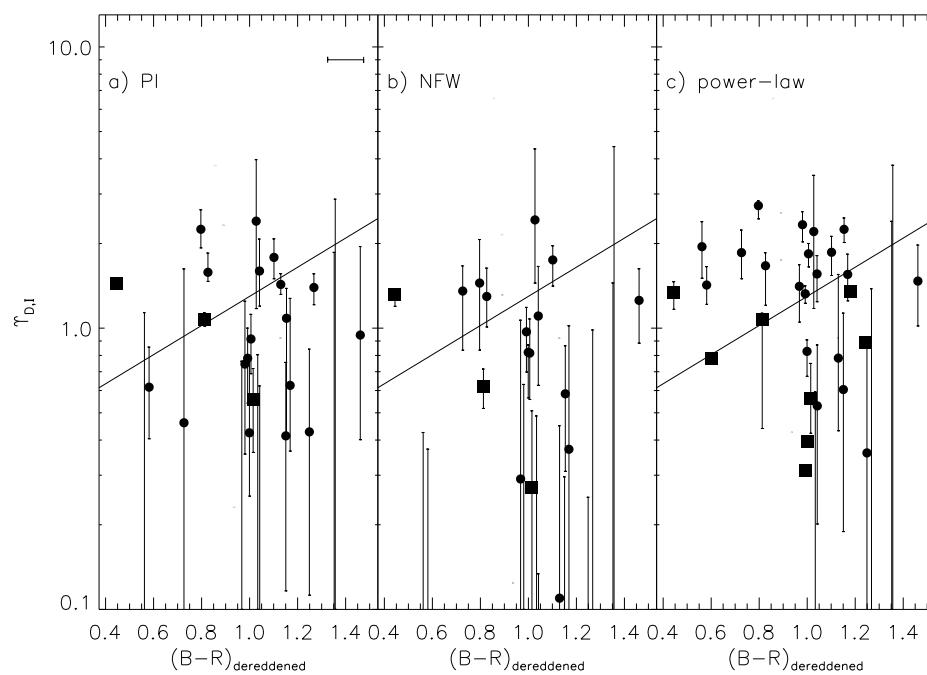


Fig. 7.— Fitted  $\Upsilon_{D,I}$  values vs. dereddened  $B - R$  when halos are included. The solid line in each panel is the best-fit correlation found by Bell *et al.* (2003). As in Figure 2(a), the solid squares denote galaxies without bulges. The error bars shown are the statistical errors presented in the tables, and do not include systematic errors. The horizontal error bar in the upper right corner of panel a) is the estimated color uncertainty for each galaxy.

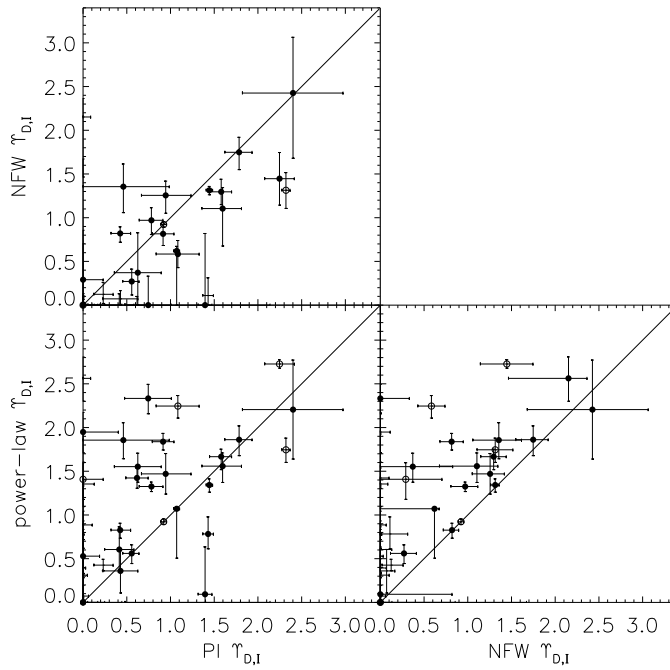


Fig. 8.— Comparisons between the  $\Upsilon_{D,I}$  values fitted for the different halo models. Filled points mark galaxies which have  $\Upsilon_{D,I} > 0.5$  for both of the relevant models. Open circles indicate galaxies which do not require halos for either of the models.

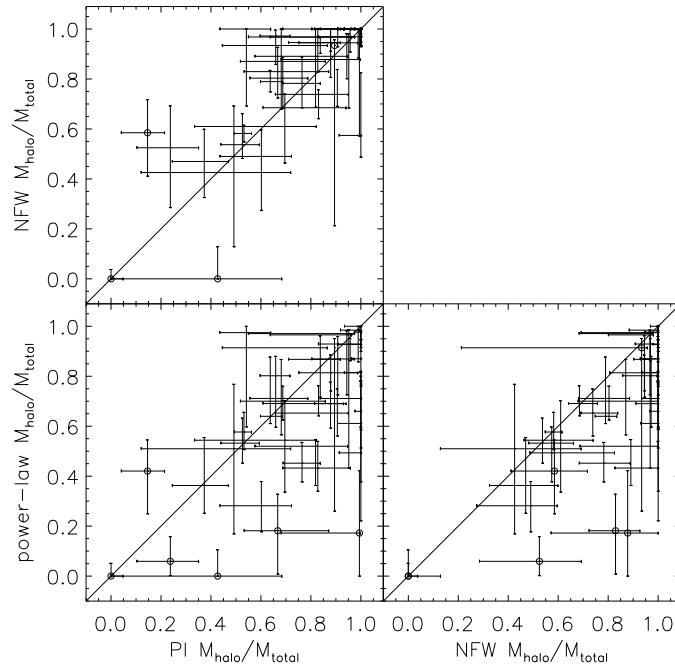


Fig. 9.— Comparisons between the fractional halo masses for the different halo models. Open and filled points have the same meanings as in Figure 8.

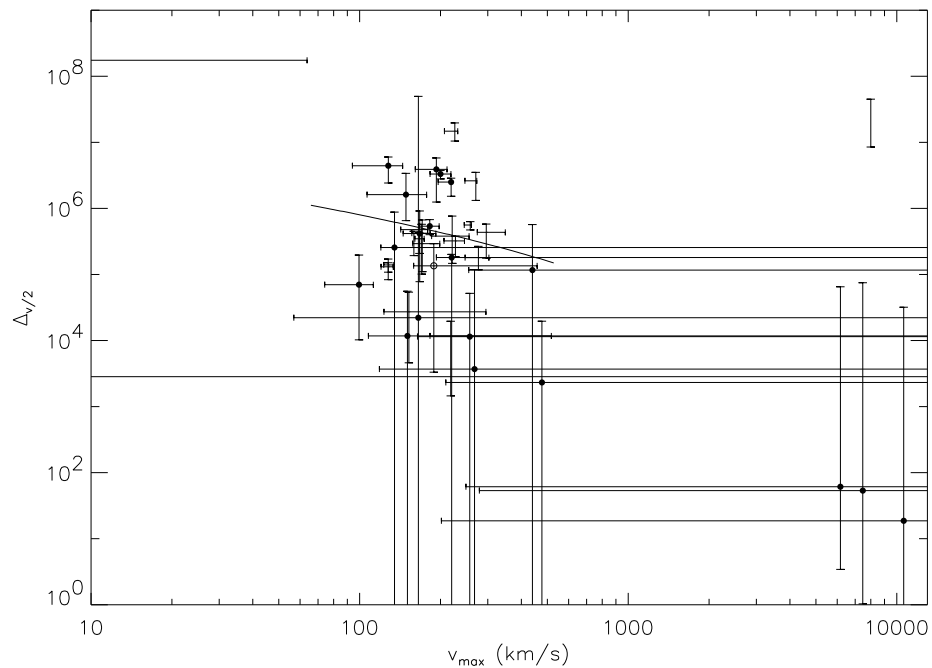


Fig. 10.— Inner halo densities ( $\Delta_{v/2}$ ) as a function of maximum halo velocity for the NFW halo function. Filled circles denote galaxies which have best-fit  $\Upsilon_{D,I} > 0.5$ , the open circle is for a galaxy for which no halo is required, and the points with error bars, but no circle are those for which  $\Upsilon_{D,I} < 0.5$ . The large error bars are for galaxies for which  $r_s$  is poorly constrained by our data. The solid line is the predicted correlation from Zentner & Bullock (2002) and the error bar in the upper right hand corner is the  $\Delta_{v/2}$  uncertainty estimated from Bullock *et al.* (2001).

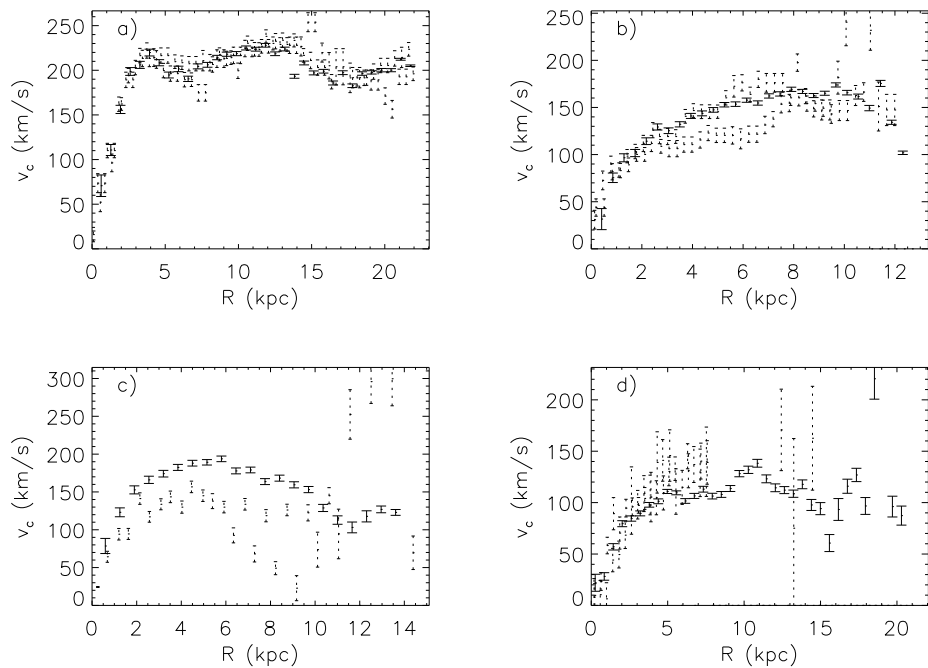


Fig. 11.— Comparisons between velocity map rotation curves (solid error bars) and pseudo-slit rotation curves (dotted error bars) for 4 galaxies. (a) ESO 322g82 is an example of good agreement between the rotation curves. (b) ESO 322g36 has strong spirals which cause a difference between the approaching and receding sides of the pseudo-slit data. (c) ESO 438g08, the poor correspondence between the two curves arises because the photometric major axis is misaligned from the kinematic major axis. (d) ESO 501g01: the data along the major axis simply does not extend to large radius.

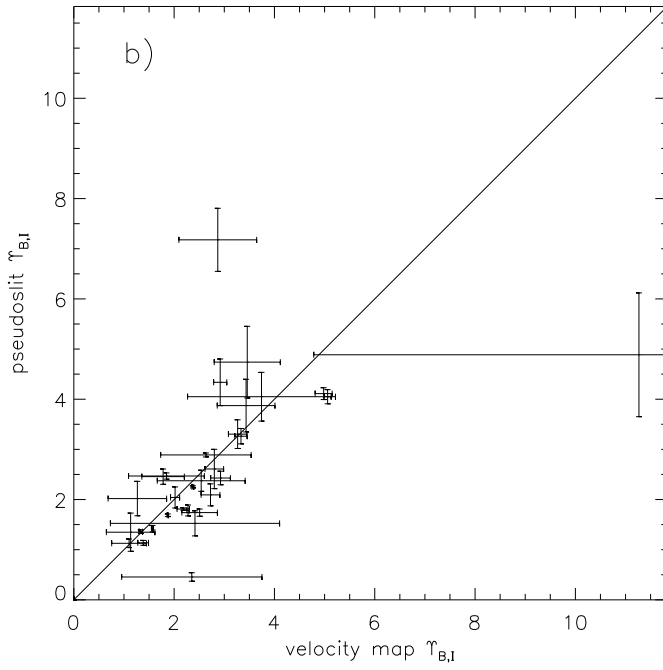
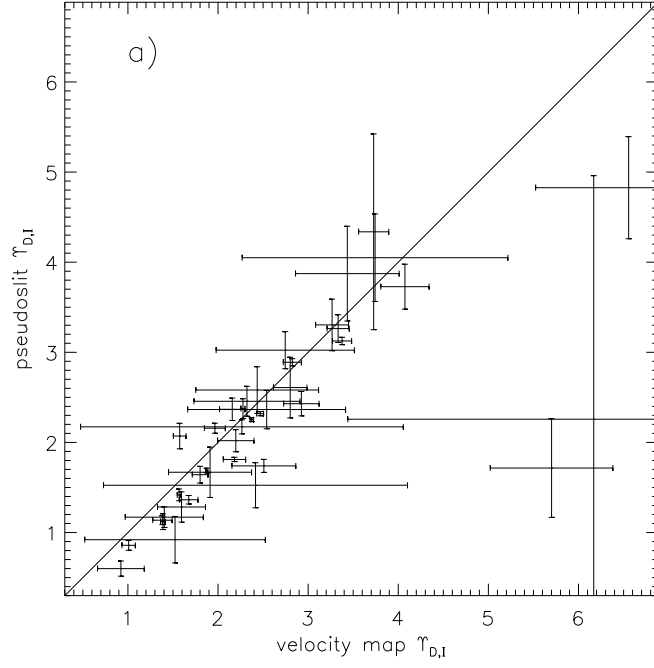


Fig. 12.— Comparisons between stars-only velocity map  $\Upsilon_I$  values and pseudo-slit  $\Upsilon_I$  values.

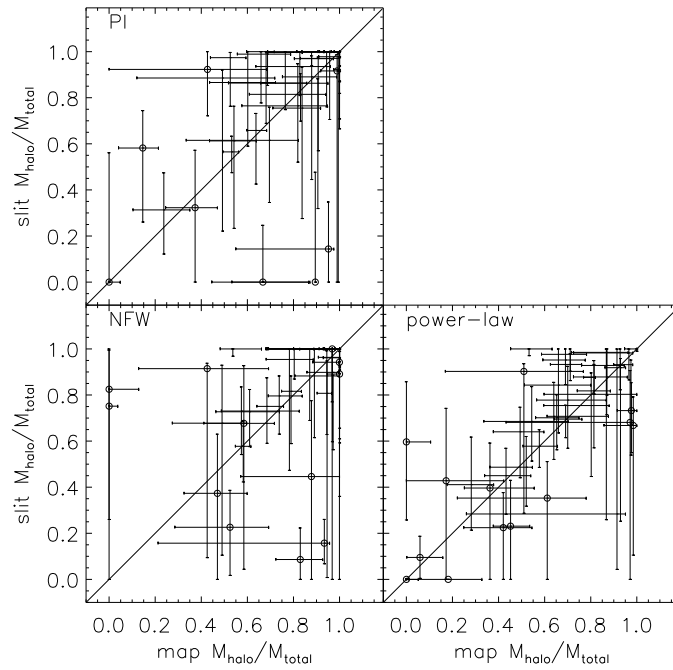


Fig. 13.— Comparisons of the dark matter halo masses for each of the halo models derived using pseudo-slit versus map data. Open circles indicate galaxies which do not require halos for either the pseudo-slit or velocity map fit.



TABLE 1

PALUNAS &amp; WILLIAMS (2000) GALAXIES REJECTED FOR THIS STUDY AND REASONS FOR EXCLUSION.

Galaxy	Galaxy	Galaxy
Abell 1644d83 <sup>1</sup>	ESO 377g11 <sup>3</sup>	ESO 444g21 <sup>1</sup>
ESO 216g20 <sup>2</sup>	ESO 381g51 <sup>1</sup>	ESO 444g86 <sup>1</sup>
ESO 267g30 <sup>1</sup>	ESO 382g58 <sup>1,3</sup>	ESO 445g35 <sup>3</sup>
ESO 269g61 <sup>1</sup>	ESO 383g02 <sup>3</sup>	ESO 445g58 <sup>2,3</sup>
ESO 322g19 <sup>1</sup>	ESO 383g88 <sup>3</sup>	ESO 445g81 <sup>1</sup>
ESO 322g48 <sup>1</sup>	ESO 435g50 <sup>1</sup>	ESO 501g11 <sup>1</sup>
ESO 322g87 <sup>1</sup>	ESO 436g39 <sup>1</sup>	ESO 501g15 <sup>2,3</sup>
ESO 374g02 <sup>3</sup>	ESO 437g30 <sup>1</sup>	ESO 501g86 <sup>2</sup>
ESO 375g12 <sup>3</sup>	ESO 437g34 <sup>2</sup>	ESO 509g91 <sup>1</sup>
ESO 375g29 <sup>1</sup>	ESO 437g54 <sup>1</sup>	ESO 510g11 <sup>3</sup>
ESO 376g02 <sup>1</sup>	ESO 441g22 <sup>3</sup>	ESO 572g17 <sup>3</sup>
ESO 376g10 <sup>1,2,3</sup>		

<sup>1</sup> inclination > 75°<sup>2</sup> sparse H $\alpha$  emission<sup>3</sup> lack of central H $\alpha$  emission

TABLE 2

BEST-FIT  $\chi_{b,\min}^2$  VALUES, PARAMETER VALUES, AND UNCERTAINTIES FOR STARS-ONLY MODELS.

#	Galaxy	$\chi_{b,\min}^2$	$\Upsilon_{D,I}(M_{\odot}/L_{\odot})$	$\sigma_{\Upsilon_{D,I}}$	$\Upsilon_{B,I}(M_{\odot}/L_{\odot})$	$\sigma_{\Upsilon_{B,I}}$
1	ESO 215g39	1.5836	2.32	0.59	1.78	0.42
2	ESO 216g20	4.4338	2.18	0.12	2.18	0.12
3	ESO 263g14	2.1086	1.01	0.07	...	...
4	ESO 267g29	5.6170	2.42	1.69	2.42	1.69
5	ESO 268g37	4.8726	2.43	0.68	...	...
6	ESO 268g44	2.0330	1.57	0.07	2.73	0.19
7	ESO 317g41	4.5788	2.47	0.04	1.34	0.03
8	ESO 322g36/NGC 4575	4.9430	1.40	0.43	1.10	0.35
9	ESO 322g42	4.1576	1.39	0.03	...	...
10	ESO 322g44	2.4256	1.38	0.11	1.38	0.11
11	ESO 322g45	2.5188	1.87	0.01	1.87	0.01
12	ESO 322g76	2.0912	2.16	0.14	1.13	0.48
13	ESO 322g77/NGC 4696a	3.3364	3.38	0.11	1.85	0.76
14	ESO 322g82/NGC 4679	4.0750	2.82	0.10	2.63	0.90
15	ESO 323g25	2.7170	2.75	0.77	11.27	6.48
16	ESO 323g27	2.8732	1.96	0.12	5.06	0.07
17	ESO 323g39	5.1232	1.52	1.00	...	...
18	ESO 323g42	1.5962	1.57	0.02	1.57	0.02
19	ESO 323g73	3.6364	1.59	0.27	...	...
20	ESO 374g03	3.4210	1.80	0.09	...	...
21	ESO 375g02/IC 2559	2.2998	2.20	0.20	1.27	0.58
22	ESO 381g05	3.0762	6.17	2.73	...	...
23	ESO 382g06	2.4402	6.56	1.03	3.46	0.66
24	ESO 435g26/NGC 3095	11.8916	2.54	0.88	2.54	0.88
25	ESO 437g04	3.2496	2.92	0.20	2.92	0.20
26	ESO 437g31	1.2074	3.74	1.47	3.74	1.47
27	ESO 438g08	2.0276	0.92	0.26	2.35	1.40
28	ESO 438g15	2.7118	1.67	0.10	2.02	0.09
29	ESO 439g18	4.5172	2.51	0.35	2.51	0.35
30	ESO 439g20	2.0360	3.33	0.12	3.33	0.12
31	ESO 444g47	2.0842	3.27	0.18	3.27	0.18
32	ESO 445g15	3.3342	2.80	0.19	2.80	0.19
33	ESO 445g19/IC 4319	2.4596	2.28	0.02	2.28	0.02
34	ESO 445g39/NGC 5298	4.2358	5.70	0.68	2.87	0.78
35	ESO 446g01	2.6448	1.91	0.46	...	...
36	ESO 501g01	1.9834	3.34	0.72	3.34	0.72
37	ESO 501g68	2.1836	4.07	0.27	4.98	0.17
38	ESO 502g02/NGC 3463	1.9144	2.37	0.02	2.37	0.02
39	ESO 509g80/IC 4298	3.6484	3.73	0.17	2.92	0.13
40	ESO 569g17/NGC 3453	1.6434	2.26	1.79	...	...

TABLE 2—*Continued*

#	Galaxy	$\chi^2_{b,\min}$	$\Upsilon_{D,I}(\text{M}_\odot/\text{L}_\odot)$	$\sigma_{\Upsilon_{D,I}}$	$\Upsilon_{B,I}(\text{M}_\odot/\text{L}_\odot)$	$\sigma_{\Upsilon_{B,I}}$
Maximum allowed $\Upsilon_I$ values from fits with the outer data discarded.						
10	ESO 322g44	2.1920	0.98	0.04	0.98	0.04
19	ESO 323g73	1.1802	1.31	0.24	...	...
25	ESO 437g04	3.2294	2.47	0.24	2.47	0.24
31	ESO 444g47	1.2608	2.67	0.06	2.67	0.06
35	ESO 446g01	1.1288	1.67	0.47	...	...

TABLE 3  
BEST-FIT  $b^2$  VALUES, PARAMETER VALUES, AND UNCERTAINTIES FOR PI MODELS.

Galaxy	$b^2$	$\Upsilon_{D,I}(M_{\odot}/L_{\odot})$	$\Upsilon_{B,I}(M_{\odot}/L_{\odot})$	$\rho_0 (M_{\odot}/\text{pc}^3)$	$r_c$ (kpc)	$v_{\infty}$ (km/s) <sup>a</sup>
1	1.3822	1.5e-06 <sup>0.36</sup> <sub>1.3e-06</sub>	1.50 <sup>1.50</sup> <sub>1.50</sub>	0.21 <sup>0.28</sup> <sub>0.12</sub>	1.7 <sup>1.1</sup> <sub>0.6</sub>	176.46
2	4.0878	0.95 <sup>1.01</sup> <sub>0.54</sub>	2.12 <sup>0.47</sup> <sub>0.58</sub>	7.6e-02 <sup>9.2e-02</sup> <sub>6.7e-02</sub>	4.0 <sup>121.8</sup> <sub>1.5</sub>	258.44
3	1.8988	0.56 <sup>0.16</sup> <sub>0.19</sub>	...	0.11 <sup>0.19</sup> <sub>7.0e-02</sub>	2.0 <sup>1.7</sup> <sub>0.7</sub>	152.39
4	5.3118	1.60 <sup>0.48</sup> <sub>0.40</sub>	1.95 <sup>0.78</sup> <sub>1.01</sub>	3.1e-02 <sup>5.3e-02</sup> <sub>1.8e-02</sub>	6.9 <sup>14.2</sup> <sub>3.9</sub>	286.14
5	3.9596	9.2e-07 <sup>0.29</sup> <sub>8.8e-07</sub>	...	0.20 <sup>3.7e-02</sup> <sub>7.0e-02</sub>	1.7 <sup>0.3</sup> <sub>0.1</sub>	181.35
6	1.9840	1.2e-08 <sup>0.76</sup> <sub>1.2e-08</sub>	0.28 <sup>1.45</sup> <sub>0.28</sub>	2.32 <sup>2.48</sup> <sub>1.54</sub>	0.4 <sup>0.3</sup> <sub>0.1</sub>	151.97
7	4.5604*	2.32 <sup>0.10</sup> <sub>9.1e-02</sub>	1.43 <sup>0.18</sup> <sub>0.21</sub>	1.9e-03 <sup>9.9e-04</sup> <sub>1.2e-03</sub>	1.2e+04 <sup>0.8</sup> <sub>11.7</sub>	1.2e+05
8	4.4864	0.23 <sup>0.27</sup> <sub>0.23</sub>	0.77 <sup>0.33</sup> <sub>0.34</sub>	0.13 <sup>0.11</sup> <sub>6.9e-02</sub>	2.2 <sup>1.0</sup> <sub>0.6</sub>	185.04
9	3.3828	1.1e-07 <sup>0.10</sup> <sub>5.7e-08</sub>	...	2.9e-02 <sup>4.2e-03</sup> <sub>5.6e-03</sub>	4.1 <sup>0.6</sup> <sub>0.3</sub>	161.18
10	1.5610	0.42 <sup>0.36</sup> <sub>0.17</sub>	0.42 <sup>0.36</sup> <sub>0.17</sub>	0.32 <sup>1.91</sup> <sub>0.30</sub>	0.9 <sup>2.2</sup> <sub>0.6</sub>	123.76
11	2.0248	1.40 <sup>0.17</sup> <sub>0.18</sub>	0.90 <sup>0.90</sup> <sub>0.75</sub>	1.2e-02 <sup>3.4e-03</sup> <sub>3.2e-03</sub>	2.6e+04 <sup>1.2e+06</sup> <sub>2.6e+04</sub>	6.5e+05
12	2.0442	1.58 <sup>0.27</sup> <sub>0.11</sub>	1.69 <sup>0.22</sup> <sub>0.32</sub>	6.0e-03 <sup>3.3e-03</sup> <sub>3.3e-03</sub>	15.2 <sup>3.0e+03</sup> <sub>6.9</sub>	272.67
13	3.0918	2.0e-05 <sup>1.86</sup> <sub>1.9e-05</sub>	4.19 <sup>0.81</sup> <sub>2.26</sub>	0.27 <sup>0.57</sup> <sub>0.22</sub>	2.5 <sup>5.8</sup> <sub>1.4</sub>	305.55
14	4.0594	2.25 <sup>0.39</sup> <sub>0.32</sub>	2.77 <sup>0.79</sup> <sub>0.65</sub>	0.20 <sup>1.37</sup> <sub>0.19</sub>	0.9 <sup>1.8</sup> <sub>0.5</sub>	94.99
15	2.5246	0.92 <sup>0.20</sup> <sub>0.23</sub>	0.92 <sup>0.20</sup> <sub>0.23</sub>	1.98 <sup>0.42</sup> <sub>0.31</sub>	0.6 <sup>5.3e-02</sup> <sub>6.5e-02</sub>	207.34
16	2.6860	8.0e-07 <sup>0.80</sup> <sub>8.0e-07</sub>	2.89 <sup>0.96</sup> <sub>1.44</sub>	0.17 <sup>0.53</sup> <sub>6.1e-02</sub>	2.5 <sup>0.7</sup> <sub>1.5</sub>	239.32
17	4.3368	7.6e-08 <sup>0.17</sup> <sub>7.6e-08</sub>	...	4.0e-02 <sup>1.4e-02</sup> <sub>1.5e-02</sub>	2.9 <sup>0.9</sup> <sub>0.5</sub>	136.76
18	1.5142	0.78 <sup>0.22</sup> <sub>0.24</sub>	0.78 <sup>0.22</sup> <sub>0.24</sub>	8.0e-02 <sup>6.7e-02</sup> <sub>4.2e-02</sub>	1.8 <sup>0.5</sup> <sub>0.3</sub>	118.18
19	2.8006	1.07 <sup>6.3e-02</sup> <sub>5.6e-02</sub>	...	2.0e-02 <sup>2.2e-03</sup> <sub>1.8e-03</sub>	1.7e+04 <sup>4.4e+05</sup> <sub>1.7e+04</sub>	5.6e+05
20	3.1678	1.6e-07 <sup>3.9e-02</sup> <sub>1.5e-07</sub>	...	0.10 <sup>1.4e-02</sup> <sub>1.3e-02</sub>	1.8 <sup>0.2</sup> <sub>0.1</sub>	135.16
21	2.0276	1.43 <sup>0.13</sup> <sub>0.11</sub>	2.62 <sup>0.52</sup> <sub>0.47</sub>	1.4e-02 <sup>2.1e-03</sup> <sub>1.9e-03</sub>	3.9e+04 <sup>2.4e+06</sup> <sub>3.9e+04</sub>	1.1e+06
22	2.2082	5.9e-08 <sup>0.26</sup> <sub>2.2e-08</sub>	...	0.50 <sup>0.11</sup> <sub>9.1e-02</sub>	1.7 <sup>0.2</sup> <sub>0.2</sub>	287.02
23	2.4352*	3.79 <sup>3.36</sup> <sub>2.89</sub>	1.94 <sup>1.95</sup> <sub>1.42</sub>	0.11 <sup>1.3e+04</sup> <sub>0.11</sub>	1.5 <sup>5.5</sup> <sub>1.5</sub>	117.94
24	11.8492	1.08 <sup>0.30</sup> <sub>0.67</sub>	1.51 <sup>1.41</sup> <sub>0.89</sub>	0.16 <sup>8.8e-02</sup> <sub>4.5e-02</sub>	1.9 <sup>0.3</sup> <sub>0.3</sub>	174.89
25	2.4646	1.7e-06 <sup>0.62</sup> <sub>1.7e-06</sub>	9.8e-07 <sup>0.18</sup> <sub>9.7e-07</sub>	0.23 <sup>3.6e-02</sup> <sub>9.2e-02</sub>	2.3 <sup>0.6</sup> <sub>0.2</sub>	253.65
26	1.0336	1.8e-08 <sup>0.34</sup> <sub>1.8e-08</sub>	1.8e-08 <sup>0.34</sup> <sub>1.8e-08</sub>	0.19 <sup>3.2e-02</sup> <sub>4.1e-02</sub>	1.5 <sup>0.1</sup> <sub>0.1</sub>	151.99
27	2.0276*	0.92 <sup>5.7e-02</sup> <sub>6.6e-02</sub>	2.35 <sup>0.61</sup> <sub>0.63</sub>	3.6e-07 <sup>2.0e+09</sup> <sub>3.6e-07</sub>	9.4e-02 <sup>5.6</sup> <sub>9.4e-02</sub>	0.01
28	2.5456	0.43 <sup>0.41</sup> <sub>0.32</sub>	1.92 <sup>0.24</sup> <sub>0.18</sub>	1.5e-02 <sup>1.0e-02</sup> <sub>8.6e-03</sub>	9.8 <sup>36.9</sup> <sub>3.2</sub>	282.29
29	3.8966	0.62 <sup>0.24</sup> <sub>0.21</sub>	0.62 <sup>0.24</sup> <sub>0.21</sub>	0.46 <sup>0.28</sup> <sub>0.17</sub>	1.7 <sup>0.4</sup> <sub>0.3</sub>	266.99
30	1.7666	0.75 <sup>0.50</sup> <sub>0.39</sub>	0.75 <sup>0.50</sup> <sub>0.39</sub>	0.80 <sup>0.36</sup> <sub>0.31</sub>	1.0 <sup>0.2</sup> <sub>0.1</sub>	213.50
31	1.6208	0.46 <sup>1.16</sup> <sub>0.46</sub>	0.46 <sup>1.16</sup> <sub>0.46</sub>	0.11 <sup>8.4e-02</sup> <sub>8.1e-02</sub>	2.2 <sup>1.9</sup> <sub>0.6</sub>	168.11
32	3.0656	1.78 <sup>0.29</sup> <sub>0.29</sub>	1.78 <sup>0.29</sup> <sub>0.29</sub>	0.14 <sup>0.45</sup> <sub>0.11</sub>	1.6 <sup>1.8</sup> <sub>0.8</sub>	144.76
33	2.2896	2.9e-06 <sup>0.32</sup> <sub>2.8e-06</sub>	1.55 <sup>0.73</sup> <sub>0.72</sub>	0.19 <sup>5.0e-02</sup> <sub>5.1e-02</sub>	2.4 <sup>0.4</sup> <sub>0.3</sub>	241.52
34	4.1728	3.3e-06 <sup>2.88</sup> <sub>3.3e-06</sub>	3.29 <sup>1.09</sup> <sub>1.38</sub>	0.22 <sup>0.17</sup> <sub>0.12</sub>	3.7 <sup>1.9</sup> <sub>1.4</sub>	404.20
35	2.2198	1.44 <sup>5.9e-02</sup> <sub>6.0e-02</sub>	...	1.1e-02 <sup>4.6e-03</sup> <sub>3.3e-03</sub>	9.7 <sup>4.3</sup> <sub>2.1</sub>	233.82
36	2.2832	7.2e-10 <sup>1.14</sup> <sub>2.9e-18</sub>	6.7e-07 <sup>0.64</sup> <sub>4.4e-07</sub>	8.9e-02 <sup>1.7e-02</sup> <sub>4.7e-02</sub>	2.0 <sup>0.5</sup> <sub>0.2</sub>	136.94
37	2.1342	2.40 <sup>1.57</sup> <sub>1.23</sub>	2.79 <sup>2.19</sup> <sub>1.33</sub>	4.99 <sup>3.4e+07</sup> <sub>4.99</sub>	0.2 <sup>10.7</sup> <sub>0.2</sub>	117.32
38	1.6984	0.63 <sup>0.65</sup> <sub>0.26</sub>	0.63 <sup>0.65</sup> <sub>0.26</sub>	2.18 <sup>1.99</sup> <sub>1.63</sub>	0.6 <sup>0.4</sup> <sub>0.1</sub>	191.69
39	3.4298	0.41 <sup>0.34</sup> <sub>0.30</sub>	0.41 <sup>0.34</sup> <sub>0.30</sub>	0.27 <sup>4.9e-02</sup> <sub>5.3e-02</sub>	2.2 <sup>0.2</sup> <sub>0.1</sub>	265.12
40	1.4480	6.1e-10 <sup>0.30</sup> <sub>6.1e-10</sub>	...	8.24 <sup>2.88</sup> <sub>2.05</sub>	0.4 <sup>4.9e-02</sup> <sub>5.4e-02</sub>	243.78

<sup>a</sup> $v_\infty$  is not a fitted parameter. It has been calculated using the best-fit  $\rho_0$  and  $r_c$  values to facilitate comparison with the other halos' velocity parameters.

\*Indicates that the halo fit is no better than the stars-only fit at the 95% level.

TABLE 4  
BEST-FIT  $b^2$  VALUES, PARAMETER VALUES, AND UNCERTAINTIES FOR NFW MODELS.

Galaxy	$b^2$	$\Upsilon_{D,I}(M_{\odot}/L_{\odot})$	$\Upsilon_{B,I}(M_{\odot}/L_{\odot})$	c	$v_{200}$ (km/s)	$r_s$ (kpc) <sup>a</sup>
1	1.3946	3.9e-07 <sup>0.15</sup> <sub>3.3e-07</sub>	1.13 <sup>1.18</sup> <sub>1.13</sub>	15.6 <sup>7.45</sup> <sub>5.16</sub>	127.3 <sup>29.7</sup> <sub>20.6</sub>	10.9
2	4.1132	1.26 <sup>0.37</sup> <sub>0.37</sub>	1.55 <sup>0.39</sup> <sub>0.43</sub>	6.0e-02 <sup>6.23</sup> <sub>5.9e-02</sub>	3.8e+03 <sup>1.7e+03</sup> <sub>3.6e+03</sub>	8.5e+04
3	1.9000	0.27 <sup>0.24</sup> <sub>0.19</sub>	...	17.9 <sup>7.55</sup> <sub>10.2</sub>	120.0 <sup>55.0</sup> <sub>16.8</sub>	8.9
4	5.3142	1.10 <sup>0.55</sup> <sub>0.48</sub>	1.97 <sup>0.94</sup> <sub>0.78</sub>	0.15 <sup>8.85</sup> <sub>0.15</sub>	4.0e+03 <sup>2.0e+03</sup> <sub>3.8e+03</sub>	3.5e+04
5	4.0182	5.0e-08 <sup>0.25</sup> <sub>3.6e-08</sub>	...	16.7 <sup>2.43</sup> <sub>3.06</sub>	122.0 <sup>8.3</sup> <sub>7.5</sub>	9.8
6	1.9934	0.29 <sup>0.78</sup> <sub>0.29</sub>	0.29 <sup>0.78</sup> <sub>0.29</sub>	44.3 <sup>18.73</sup> <sub>9.46</sub>	69.6 <sup>7.7</sup> <sub>24.7</sub>	2.1
7	4.6242*	1.31 <sup>0.39</sup> <sub>0.24</sub>	1.31 <sup>0.39</sup> <sub>0.24</sub>	11.5 <sup>6.68</sup> <sub>7.25</sub>	151.9 <sup>79.1</sup> <sub>31.2</sub>	17.7
8	4.4812	0.12 <sup>0.26</sup> <sub>0.12</sub>	0.12 <sup>0.47</sup> <sub>0.12</sub>	18.0 <sup>4.38</sup> <sub>7.78</sub>	121.9 <sup>31.7</sup> <sub>11.3</sub>	9.0
9	3.5878	1.0e-06 <sup>0.20</sup> <sub>1.0e-06</sub>	...	4.06 <sup>2.35</sup> <sub>2.33</sub>	210.9 <sup>191.0</sup> <sub>69.7</sub>	69.3
10	1.5704	0.82 <sup>5.2e-02</sup> <sub>0.26</sub>	0.82 <sup>5.2e-02</sup> <sub>0.26</sub>	4.05 <sup>12.02</sup> <sub>2.60</sub>	145.5 <sup>163.2</sup> <sub>64.6</sub>	47.9
11	2.0276	1.4e-06 <sup>0.98</sup> <sub>8.1e-07</sub>	1.4e-05 <sup>1.30</sup> <sub>1.3e-05</sub>	12.9 <sup>4.42</sup> <sub>11.9</sub>	172.2 <sup>1.2e+03</sup> <sub>37.5</sub>	17.8
12	2.0502	1.30 <sup>0.34</sup> <sub>0.29</sub>	1.58 <sup>0.27</sup> <sub>0.27</sub>	5.7e-04 <sup>2.52</sup> <sub>5.6e-04</sub>	1.6e+03 <sup>770.4</sup> <sub>1.2e+03</sub>	3.7e+06
13	3.0854	1.6e-06 <sup>1.45</sup> <sub>1.5e-06</sub>	2.86 <sup>1.02</sup> <sub>1.57</sub>	10.8 <sup>17.65</sup> <sub>9.40</sub>	358.8 <sup>3.0e+03</sup> <sub>223.1</sub>	44.4
14	4.0478	1.45 <sup>0.62</sup> <sub>0.61</sub>	1.42 <sup>1.05</sup> <sub>1.21</sub>	30.3 <sup>13.11</sup> <sub>11.7</sub>	91.5 <sup>13.8</sup> <sub>17.3</sub>	4.0
15	2.4916	0.82 <sup>0.26</sup> <sub>0.26</sub>	0.82 <sup>0.26</sup> <sub>0.26</sub>	39.8 <sup>4.02</sup> <sub>3.65</sub>	112.7 <sup>7.8</sup> <sub>7.5</sub>	3.8
16	2.6952	4.5e-07 <sup>0.49</sup> <sub>4.3e-07</sub>	1.71 <sup>1.03</sup> <sub>0.58</sub>	17.3 <sup>6.35</sup> <sub>5.46</sub>	160.1 <sup>40.3</sup> <sub>28.5</sub>	12.3
17	4.3938	1.0e-07 <sup>9.2e-02</sup> <sub>5.3e-08</sub>	...	5.87 <sup>5.00</sup> <sub>3.24</sub>	140.2 <sup>126.4</sup> <sub>47.0</sub>	31.8
18	1.5374	0.97 <sup>0.21</sup> <sub>0.27</sub>	0.97 <sup>0.21</sup> <sub>0.27</sub>	8.75 <sup>4.91</sup> <sub>5.42</sub>	84.9 <sup>28.2</sup> <sub>14.6</sub>	12.9
19	2.8008	0.62 <sup>9.6e-02</sup> <sub>0.10</sub>	...	0.17 <sup>8.32</sup> <sub>0.16</sub>	3.5e+03 <sup>1.2e+03</sup> <sub>3.3e+03</sub>	2.7e+04
20	3.2332	4.8e-07 <sup>5.6e-02</sup> <sub>4.6e-07</sub>	...	11.6 <sup>1.10</sup> <sub>1.11</sub>	102.5 <sup>4.9</sup> <sub>4.5</sub>	11.8
21	2.0202	0.11 <sup>0.34</sup> <sub>4.5e-02</sub>	0.11 <sup>0.34</sup> <sub>4.5e-02</sub>	18.9 <sup>2.17</sup> <sub>6.60</sub>	112.5 <sup>27.9</sup> <sub>11.6</sub>	7.9
22	2.1980	1.2e-06 <sup>0.40</sup> <sub>1.1e-06</sub>	...	18.2 <sup>3.80</sup> <sub>1.69</sub>	211.4 <sup>46.6</sup> <sub>25.8</sub>	15.5
23	2.4402*	6.56 <sup>1.07</sup> <sub>1.45</sub>	3.46 <sup>0.66</sup> <sub>0.80</sub>	2.06 <sup>4.97</sup> <sub>2.06</sub>	2.6e-03 <sup>182.0</sup> <sub>2.6e-03</sub>	0.0
24	11.8384	0.58 <sup>0.28</sup> <sub>0.27</sub>	0.58 <sup>0.28</sup> <sub>0.27</sub>	19.8 <sup>2.40</sup> <sub>2.40</sub>	127.2 <sup>6.3</sup> <sub>7.0</sub>	8.6
25	2.5360	1.5e-06 <sup>0.13</sup> <sub>1.4e-06</sub>	1.5e-06 <sup>0.13</sup> <sub>1.4e-06</sub>	12.8 <sup>1.53</sup> <sub>1.94</sub>	216.6 <sup>29.7</sup> <sub>18.2</sub>	22.5
26	1.0658	2.15 <sup>0.15</sup> <sub>1.29</sub>	2.15 <sup>0.15</sup> <sub>1.29</sub>	2.35 <sup>10.31</sup> <sub>1.10</sub>	267.6 <sup>144.0</sup> <sub>168.2</sub>	1.5e+02
27	2.0276*	0.92 <sup>6.3e-02</sup> <sub>6.4e-02</sub>	2.35 <sup>0.41</sup> <sub>0.70</sub>	171.4 <sup>0.21</sup> <sub>81.1</sub>	8.0e-02 <sup>21.6</sup> <sub>8.0e-02</sub>	0.0
28	2.5472	7.2e-02 <sup>0.18</sup> <sub>7.2e-02</sub>	1.22 <sup>0.11</sup> <sub>0.20</sub>	1.8e-04 <sup>5.11</sup> <sub>1.4e-04</sub>	3.1e+03 <sup>20.7</sup> <sub>2.8e+03</sub>	2.3e+07
29	3.9182	2.8e-06 <sup>0.37</sup> <sub>2.7e-06</sub>	2.8e-06 <sup>0.37</sup> <sub>2.7e-06</sub>	36.3 <sup>4.18</sup> <sub>6.87</sub>	157.1 <sup>4.1</sup> <sub>5.5</sub>	5.8
30	1.7894	5.1e-07 <sup>0.63</sup> <sub>5.1e-07</sub>	5.1e-07 <sup>0.63</sup> <sub>5.1e-07</sub>	35.8 <sup>2.26</sup> <sub>5.95</sub>	127.8 <sup>2.8</sup> <sub>6.6</sub>	4.8
31	1.6606	1.36 <sup>0.31</sup> <sub>0.52</sub>	1.36 <sup>0.31</sup> <sub>0.52</sub>	4.01 <sup>6.05</sup> <sub>2.71</sub>	248.6 <sup>350.8</sup> <sub>122.2</sub>	82.7
32	3.0718	1.75 <sup>0.21</sup> <sub>0.34</sub>	1.75 <sup>0.21</sup> <sub>0.34</sub>	14.8 <sup>19.36</sup> <sub>9.90</sub>	101.8 <sup>94.2</sup> <sub>22.4</sub>	9.2
33	2.2710	1.2e-07 <sup>0.23</sup> <sub>1.2e-07</sub>	9.8e-02 <sup>0.54</sup> <sub>9.8e-02</sub>	16.2 <sup>2.62</sup> <sub>4.00</sub>	167.6 <sup>27.4</sup> <sub>19.6</sub>	13.8
34	4.2076*	1.4e-04 <sup>4.42</sup> <sub>1.4e-04</sub>	2.34 <sup>0.66</sup> <sub>0.75</sub>	8.8e-06 <sup>1.7e-02</sup> <sub>8.8e-06</sub>	1.5e+04 <sup>3.8e+03</sup> <sub>1.2e+04</sub>	2.3e+09
35	2.2232	1.31 <sup>0.12</sup> <sub>0.12</sub>	...	1.86 <sup>5.88</sup> <sub>1.51</sub>	476.2 <sup>775.0</sup> <sub>318.4</sub>	3.4e+02
36	2.3106	6.2e-07 <sup>0.43</sup> <sub>2.0e-07</sub>	6.2e-07 <sup>0.43</sup> <sub>2.0e-07</sub>	11.3 <sup>1.55</sup> <sub>1.80</sub>	103.1 <sup>6.1</sup> <sub>6.2</sub>	12.2
37	2.1400	2.43 <sup>1.91</sup> <sub>0.98</sub>	4.28 <sup>0.86</sup> <sub>2.85</sub>	5.37 <sup>4.8e+02</sup> <sub>5.33</sub>	154.2 <sup>152.0</sup> <sub>153.4</sub>	38.3
38	1.7024	0.37 <sup>0.65</sup> <sub>0.28</sub>	0.37 <sup>0.65</sup> <sub>0.28</sub>	42.3 <sup>10.78</sup> <sub>14.8</sub>	106.7 <sup>6.6</sup> <sub>9.5</sub>	3.4
39	3.4314	2.0e-06 <sup>0.30</sup> <sub>1.7e-06</sub>	2.0e-06 <sup>0.30</sup> <sub>1.7e-06</sub>	20.1 <sup>1.08</sup> <sub>1.50</sub>	179.2 <sup>2.5</sup> <sub>7.6</sub>	11.9
40	1.4178	9.0e-09 <sup>0.30</sup> <sub>9.0e-09</sub>	...	69.4 <sup>9.54</sup> <sub>7.85</sub>	105.5 <sup>4.4</sup> <sub>7.7</sub>	2.0

<sup>a</sup> $R_s$  is not a fitted parameter. It has been calculated using the best-fit  $v_{200}$  and  $c$  values to facilitate comparison with the PI scale length parameter.

\*Indicates that the halo fit is no better than the stars-only fit at the 95% level.

TABLE 5

BEST-FIT  $b^2$  VALUES, PARAMETER VALUES, AND UNCERTAINTIES FOR POWER MODELS.

Galaxy	$b^2$	$\Upsilon_{D,I}(M_\odot/L_\odot)$	$\Upsilon_{B,I}(M_\odot/L_\odot)$	$v_0$ (km/s)	$\alpha$
1	1.4170	9.3e-08	2.69	158.2	1.2
2	4.1074	1.47	1.79	162.5	0.7
3	1.9188	0.56	...	134.2	1.2
4	5.3118	1.56	1.56	161.8	0.8
5	4.0946	0.89	...	151.4	1.3
6	2.0340*	1.41	2.46	48.7	1.6
7	4.6356*	1.75	1.75	140.7	1.1
8	4.4868	0.43	0.43	156.5	1.4
9	3.5878	0.39	...	117.1	0.8
10	1.5710	0.83	0.83	111.8	1.2
11	2.0196	9.3e-02	9.3e-02	175.7	1.2
12	2.0456	1.67	1.63	105.5	1.4e-05
13	3.0854	4.7e-06	2.64	216.9	1.1
14	4.0674*	2.73	3.01	45.5	1.4e-07
15	2.6250	1.84	1.84	142.2	1.9
16	2.7340	2.5e-06	1.90	209.2	1.4
17	4.4164	7.8e-08	...	123.2	1.1
18	1.5448	1.33	1.33	71.2	1.0
19	2.8006	1.07	...	138.7	4.1e-06
20	3.2848	0.78	...	102.9	1.3
21	2.0262	0.78	1.35	139.0	1.1
22	2.2136	0.31	...	278.0	1.3
23	2.4402*	6.56	3.46	1.0e-02	1.1
24	11.8892*	2.25	2.25	76.2	1.5
25	2.5674	0.53	0.53	213.5	1.1
26	1.0642	2.56	2.56	94.8	0.7
27	2.0276*	0.92	2.35	2.1e-02	2.0
28	2.5464	0.36	1.64	155.1	0.7
29	4.0170	1.42	1.42	208.5	1.3
30	1.8488	2.33	2.33	140.4	1.3
31	1.6564	1.86	1.86	128.9	0.8
32	3.0768	1.86	1.86	133.4	1.4
33	2.2718	7.3e-02	7.3e-02	215.8	1.4
34	4.2046	2.0e-05	3.02	305.5	0.9
35	2.2232	1.34	...	157.9	1.0
36	2.3404	1.95	1.95	108.0	1.1
37	2.1290	2.21	3.36	118.3	1.6
38	1.7194	1.55	1.55	142.2	1.5
39	3.5774	0.60	0.60	241.9	1.6
40	1.6092	1.35	...	147.8	1.8



TABLE 5—*Continued*

Galaxy	$b^2$	$\Upsilon_{D,I}(M_{\odot}/L_{\odot})$	$\Upsilon_{B,I}(M_{\odot}/L_{\odot})$	$v_0$ (km/s)	$\alpha$
--------	-------	---------------------------------------	---------------------------------------	--------------	----------

\*Indicates that the halo fit is no better than the stars-only fit at the 95% level.